TABLE 1. Primary Antibodies

Antigen	Class	Dilution	Supplier
Anti-perlecan	Rabbit polyclonal	1/100	Seigaku, Tokyo Japan
Anti-Ki67	Rabbit polyclonal	1/200	Abcam, Cambridge UK
Anti-cytokeratin12	Goat polyclonal	1/200	Santa Cruz Biotech, Santa Cruz, CA
Anti-connexin43	Rabbit polyclonal	1/2000	Abcam
Anti-Notch1	Rabbit polyclonal	1/200	Abcam
Anti-Pax6	Mouse monoclonal	1/200	R&D Systems Minneapolis, MN

Hspg$^{+/Tg}$) were then created by mating the transgenic mice with heterozygous *Hspg2*$^{+/-}$ mice. The *Hspg2*$^{-/-}$-Tg mice exhibited normal cephalic development, and those mice were then maintained in a mixed genetic background of C57BL/6 and SVJ 129. In this study, we used 8- and 16-week-old *Hspg2*$^{-/-}$-Tg mice and *Hspg2*$^{+/+}$-Tg mice as well as wild-type (WT) mice, and the eyes of those mice were dissected and prepared for histologic or molecular analysis. All animal experiments in this study were performed in accordance with the guidelines set forth in the ARVO Statement for the Use of Animals in Ophthalmic and Vision Research.

Histologic Analysis

The excised mouse eyes were fixed in 20% formalin in phosphate-buffered saline (PBS) at 4°C overnight and then embedded in paraffin. Next, 3-μm-thick sections of the eyes were mounted on microslides (New Silane; Muto-Glass, Tokyo, Japan). Histologic examination was performed after Harris hematoxylin and eosin (H-E) staining. Histology of the corneas of the 8-week-old *Hspg2*$^{-/-}$-Tg and WT mice littermates was then compared by use of light microscopy (AX80; Olympus Corp., Tokyo, Japan).

Morphometric Measurements

For the morphometric measurements, corneal thicknesses were calculated in 8-week-old *Hspg2*$^{-/-}$-Tg and WT mice. Next, 3-μm-thick tissue sections of the cornea stained with H-E staining were viewed by light microscopy (40× magnification) with a computerized image analyzer (KS400; Carl Zeiss AG, Oberkochen, Germany), and measurements were made by use of a calibrated eyepiece graticule. Corneal thickness was measured in the central region of the serial sections of each eye. The mean thickness was then calculated by averaging those measurements. The epithelial, stromal, endothelial, and whole corneal thicknesses were then compared. The ratio of the epithelial cell layer thickness to the full corneal thickness was also calculated.

Examination by Transmission Electron Microscopy

For the transmission electron microscopy (TEM) examinations, the eyes of 8- and 16-week-old *Hspg2*$^{-/-}$-Tg and WT mice were dissected and fixed in cold 2.5% glutaraldehyde with PBS overnight at 4°C and then sectioned into small pieces. Those sections were then postfixed with 2% osmium tetroxide in the same buffer, dehydrated through a series of ethyl alcohol solutions, and embedded in Epon. All sections were examined by use of an electron microscope (H-7100; Hitachi, Tokyo, Japan) at an accelerating voltage of 75 kV.

Immunohistochemical Staining

Deparaffinized sections were washed in 100% ethanol and rehydrated with PBS. Antigen retrieval was performed by boiling the sections in 0.01 M citrate buffer (pH 6) for 10 minutes. Next, the slides were washed with PBS and blocked with 4% normal serum (species selected according to the secondary antibody) in PBS and 0.3% bovine serum albumin for 10 minutes at room temperature. The slides were incubated with primary antibody overnight at 4°C (Table 1), washed with PBS, incubated with the secondary antibodies, and counterstained with DAPI (H-1200; Vector Laboratories, Inc., Burlingame, CA). Ki67-positive cells were quantified by capturing the image of individual nuclei from *Hspg2*$^{-/-}$-Tg and WT sections processed in parallel and immunostained on the same slides. All sections were viewed with a fluorescence microscope (AxioVision 3.1; Carl Zeiss Meditec, Inc.) and confocal microscopy (TCS-SP5/TIRF; Leica Microsystems AG, Solms, Germany).

Assessment of Cell Death by TUNEL Assay

Deparaffinized sections were rehydrated through graded alcohols and then washed with PBS. The tissue sections were treated with proteinase K (80 μg/mL) for 20 minutes at room temperature. The slides were then washed twice with PBS. Next, the TUNEL assay (TUNEL in Situ Cell Death Detection Kit, fluorescein; Roche Diagnostics GmbH, Mannheim, Germany) was performed according to the manufacturer's instructions. Briefly, the sections were first counterstained with DAPI. The samples were then visualized by fluorescence microscopy, and images were obtained for quantitative analysis. TUNEL-positive cells were then quantified by capturing the image of individual nuclei from *Hspg2*$^{-/-}$-Tg and WT sections processed in parallel and immunostained on the same slides.

TABLE 2. Primers Used in RT-PCR

Gene	Primer	Primer Sequence
Ki67	Forward	5′-GCAGGAAGCAACAGATGAGAAGCC-3′
	Reverse	5′-GCTCAGGTGATACATGCCTCCTGC-3′
Active caspase3	Forward	5′-AGGTGGCAACGGAATTCGAGTC-3′
	Reverse	5′-ACACGGGATCTGTTTCTTTGCG-3′
Cytokeratin12	Forward	5′-TCTTCATGCTGGTGGTGTCCTTG-3′
	Reverse	5′-TCAAGAAACCAGGCCTCTGCATC-3′
Connexin43	Forward	5′-TCTTCATGCTGGTGGTGTCCTTG-3′
	Reverse	5′-CGATCCTTAACGCCCTTGAAGAAG-3′
Notch1	Forward	5′-GGAGGACCTCATCAACTCACATGC-3′
	Reverse	5′-CCGTTCTTCAGGAGCACAACAG-3′
Pax6	Forward	5′-AAGGATGTTGAACGGGCAGAC-3′
	Reverse	5′-TGTTGCTGGCAGCCATCTTG-3′
GAPDH	Forward	5′-AAGAGAGGCCCTATCCCAACTC-3′
	Reverse	5′-TTGTGGGTGCAGCGAACTTTATTG-3′

Analysis by Real-Time Polymerase Chain Reaction

Total RNA was isolated from the dissected corneas (NucleoSpin RNA II; Macherey-Nagel GmbH, KG, Duren, Germany) according to the manufacturer's instructions. cDNA was generated from 1.0 μg total RNA (ReverTra Ace-α; Toyobo Co., Ltd., Osaka, Japan). Real-time PCR was performed with SYBR green master mix (Fast SYBR Green Master Mix; Applied Biosystems, Inc. [ABI], Foster City, CA) on a commercial system (Prism 7500; ABI). In this study, we did not isolate the RNA from the epithelia but from the whole cornea. Therefore, the PCR analysis for the level of reduced expression of differentiation and developmental regulator molecules in *Hspg2*$^{-/-}$-Tg eyes may be semiquantitative, not absolutely quantitative. Primers sequences are listed in Table 2.

Results

Histologic Analysis of the *Hspg2*$^{-/-}$-Tg Eyes

The eyes of 8-week-old *Hspg2*$^{-/-}$-Tg mice that were approximately the same body weight and length as WT mice exhibited microphthalmos and a small palpebral fissure (Fig. 1A). Under light microscopy at low magnification, the *Hspg2*$^{-/-}$-Tg eyes stained with H-E staining also exhibited microphthalmos (Figs. 1B, 1C). Under high magnification, the *Hspg2*$^{-/-}$-Tg eyes showed a thinner corneal epithelium compared with that of the WT eyes (Figs. 1D, 1E). The localization of perlecan was examined by immunostaining with specific antibody for their core protein. Eight-week-old WT and *Hspg2*$^{-/-}$-Tg mice were stained with anti-perlecan antibody (Alexa488, green), and the corneal nuclei were stained with DAPI (blue). Perlecan was strongly expressed in the corneal epithelial BM of the WT mice (Fig. 1F). However, the expression of perlecan was not recognized in the corneal epithelium of the *Hspg2*$^{-/-}$-Tg mice (Fig. 1G).

Analysis by TEM

TEM was performed to further examine the corneal morphology in the *Hspg2*$^{-/-}$-Tg and WT mice. The corneal epithelia from WT mice and *Hspg2*$^{-/-}$-Tg, 8 weeks (Figs. 2A, 2B) and 16 weeks (Figs. 2C, 2D) of age, were analyzed by TEM. At 8 and 16 weeks of age, the *Hspg2*$^{-/-}$-Tg mice showed thinner corneal epithelia compared with the WT mice. Eight-week-old WT mice showed 9 to 10 corneal epithelial layers (Fig. 2A). In contrast, the 8-week-old *Hspg2*$^{-/-}$-Tg mice showed thinner undifferentiated wing cell layers compared with the WT mice (Fig. 2B). Corneal wing-cell layers of the 16-week-old *Hspg2*$^{-/-}$-Tg mice were thinner and undifferentiated compared with those of the WT mice. As the ages of the mice progressed, the *Hspg2*$^{-/-}$-Tg mice showed a thinner corneal epithelium compared with that of the WT mice (Fig. 2A-D). Under high magnification, no significant difference was observed between the *Hspg 2*$^{-/-}$ Tg mice and WT mice in regard to the structure of superficial cells (Figs. 2E, 2F), basal cells (Figs. 2G, 2H), and epithelial BM (Figs. 2I, 2J).

In the corneal stromal layer, the keratocytes were localized between stromal lamellae, with no significant difference found between the 8-week-old *Hspg2*$^{-/-}$-Tg and WT mice (Figs. 3A, 3B). Under high magnification, cross-sections of the collagen fibers from the *Hspg2*$^{-/-}$-Tg and WT mice demonstrated parallel bundles of a regular diameter (Figs. 3C, 3D). Under low magnification, no significant difference was observed between the *Hspg2*$^{-/-}$-Tg and WT mice as to the thickness of the endothelial layers (Figs. 3E, 3F). Under high magnification, Descemet's membrane was found to be composed of electron-dense material in both the *Hspg2*$^{-/-}$-Tg and WT mice (Figs. 3G, 3H). The corneal endothelium was found to have some

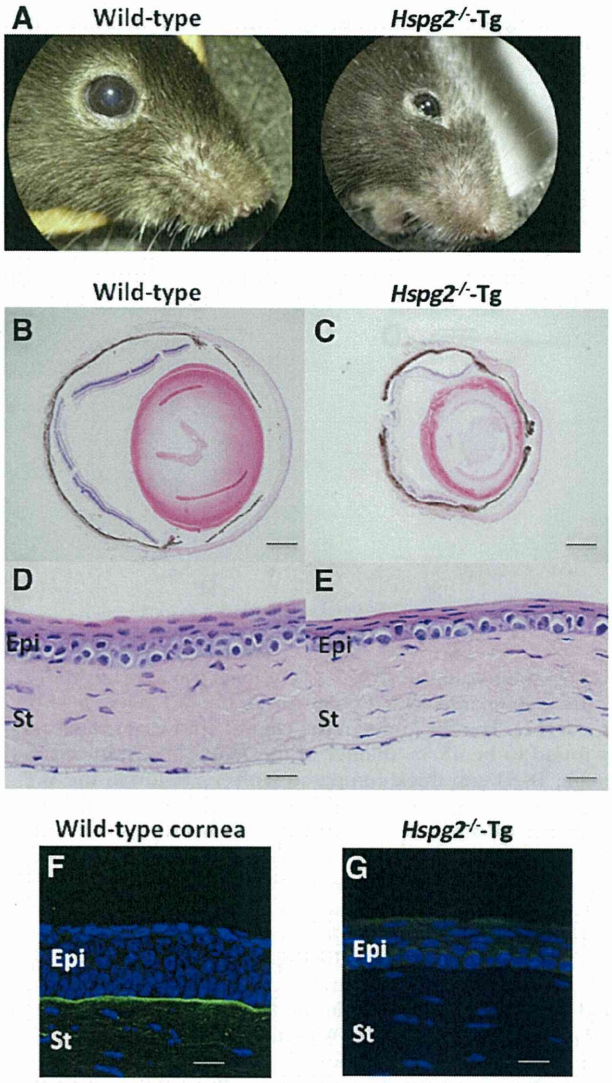

Figure 1. Histologic analysis. Representative macroscopic images of the eye in situ (**A**). H-E-stained sections (**B–E**) show the histologic features of whole eyes visualized by light microscopy at low (**B**, **C**) and high (**D**, **E**) magnifications. The 8-week-old *Hspg2*$^{-/-}$-Tg mice had microphthalmos, whereas the WT mice did not (**A–C**). The corneal epithelium of the 8-week-old *Hspg2*$^{-/-}$-Tg mice thinner than that of the WT mice (**D**, **E**). Immunohistochemical staining of perlecan in the corneas of the WT and the *Hspg2*$^{-/-}$-Tg mice (**F**, **G**). Perlecan (Alexa 488, *green*) was strongly expressed in the corneal epithelial basement membrane of the WT mice (**F**). However, the expression of perlecan was not recognized in the corneal epithelium of the *Hspg2*$^{-/-}$-Tg mice (**G**). Epi, epithelium; St, stroma. Scale bars: (**B**, **C**) 600 μm; (**D**, **E**) 40 μm; (**F**, **G**) 30 μm.

desmosomes and gap junctions, with no significant difference found between the *Hspg2*$^{-/-}$-Tg and WT mice (Figs. 3I, J).

Corneal Thickness Morphometry

The thickness of the corneal epithelium was examined in the 8-week-old mice, as that is the age at which the development of the corneal epithelium is complete. Histologic examination of those mice revealed that the corneal epithelial thickness was markedly thinned in the *Hspg2*$^{-/-}$-Tg mice. The corneal thickness of the central region was then calculated (Fig. 4A). The thickness of the central whole corneal cell layers was found to

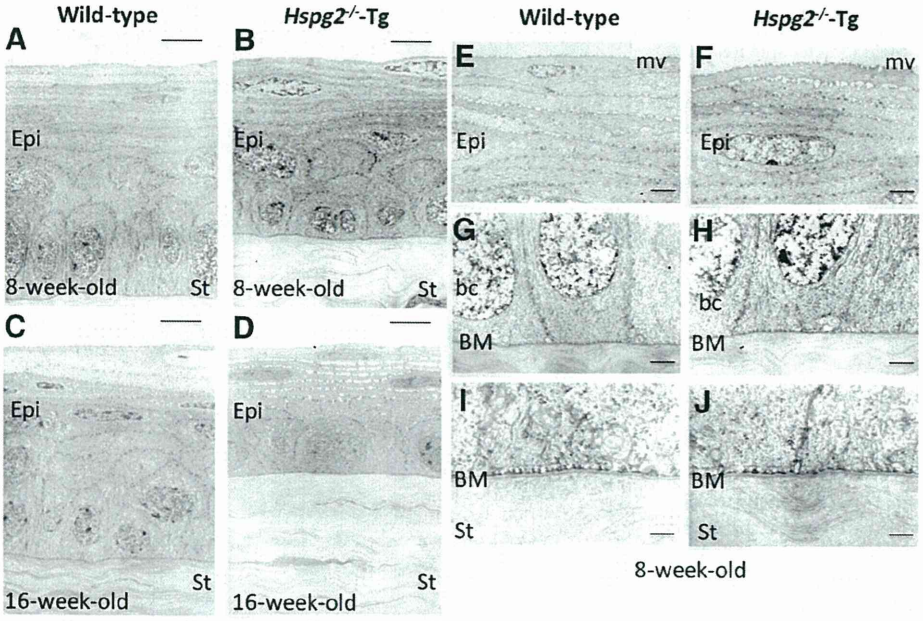

FIGURE 2. TEM of the corneal epithelium. TEM images show ultrastructural features of corneal epithelium from WT (**A**, **C**, **E**, **G**, **I**) and *Hspg2*$^{-/-}$-Tg (**B**, **D**, **F**, **H**, **J**) mice. Corneal epithelia of the 8- and 16-week-old *Hspg2*$^{-/-}$-Tg mice (**B**, **D**) were thinner and had thinner wing cell layers compared with those of the WT mice (**A**, **C**). As the ages of the mice progressed, the corneal epithelium of the 16-week-old *Hspg2*$^{-/-}$-Tg mice became thinner and the wing cell layer was undifferentiated compared with that of the WT mice (**D**). Under high magnification, no significant difference was observed between the *Hspg2*$^{-/-}$-Tg mice and WT mice in regard to the structure of the superficial cells (**E**, **F**), basal cells (**G**, **H**), and epithelial basement membrane (**I**, **J**). Epi, epithelium; St, stroma; mv, microvilli; bc, basal cell, BM, corneal basement membrane. Scale bar: (**A–D**) 5 μm; (**E-H**) 2 μm; (**I**, **J**) 0.5 μm.

be 25.6% thinner in the *Hspg2*$^{-/-}$-Tg mice (on average, 85.12 μm thick compared with 114.53 μm in the WT mice; $n = 6$; $P = 0.0411$). The thickness of the central epithelial cell layers was found to be 45.5% thinner in the *Hspg2*$^{-/-}$-Tg mice (on average, 18.51 μm thick compared with 33.94 μm in the WT mice; $n = 6$; $P = 0.0022$). The average thicknesses of the central corneal stromal layers and endothelial layers were not significantly different between the *Hspg2*$^{-/-}$-Tg and WT mice. Because of the microphthalmos of the eyes of the *Hspg2*$^{-/-}$-Tg mice, we calculated the comparison of the ratio of the epithelial cell layer thickness to the full central corneal thickness in the central region (Fig. 4B). The ratio of the central epithelial cell layer thickness to the central whole corneal thickness was found to be significant lower in the *Hspg2*$^{-/-}$-Tg mice, 22.6% compared with 29.4% in the WT mice ($n = 6$, $P = 0.0043$). These findings suggest that the corneal epithelial cell layer in the *Hspg2*$^{-/-}$-Tg mouse is thinner regardless of the microphthalmos.

Proliferation and Cell Death in *Hspg2*$^{-/-}$-Tg Corneal Epithelium

We posited that the findings of thinner corneal epithelium in the 8-week-old *Hspg2*$^{-/-}$-Tg mice could be the result of a decrease in cell proliferation or an increase in cell death. To discern between these two possibilities, immunostaining was performed to investigate the number of Ki67-positive (Figs. 5A1, A2) and TUNEL-positive (Figs. 5D1, 5D2) cells. The Ki67 antigen was designated as a marker for cell proliferation, and the number of Ki67-positive cells was scored across the entire section of the corneal epithelium. The average ratio of Ki67-positive cells to basal cells was 12% per section in the *Hspg2*$^{-/-}$-Tg epithelium, compared with 21% in the WT epithelium ($n = 6$; $P = 0.0087$; Fig. 5B). Real-time PCR for Ki67 showed a 67% decrease in RNA levels in the *Hspg2*$^{-/-}$-Tg epithelium ($n = 5$; $P = 0.0159$; Fig. 5C).

TUNEL assay assessment of cell death revealed a very small number of TUNEL-positive cells (<0.3%) per corneal section in

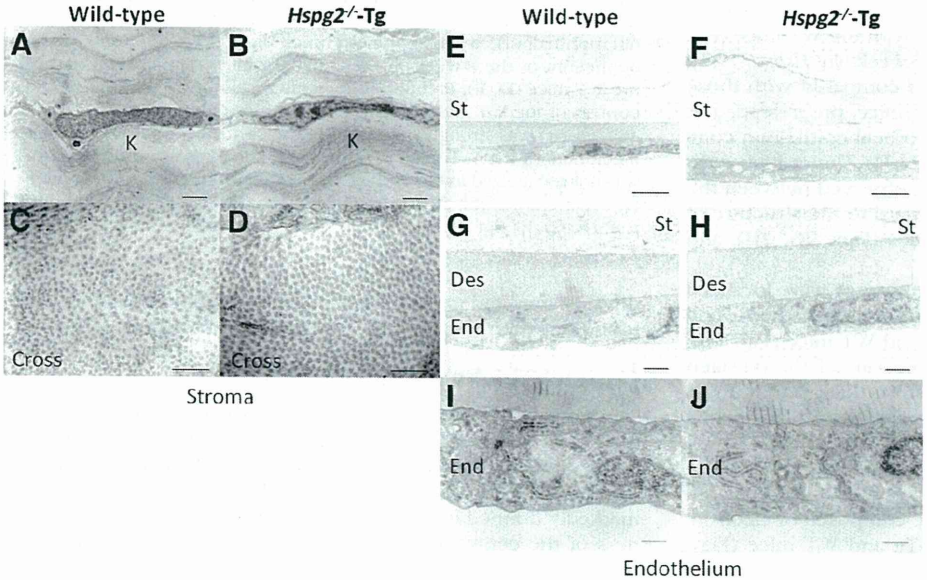

FIGURE 3. Electron microscopy of corneal stroma and endothelium. Keratocytes (**A**, **B**). Collagen fibers cut in cross-section (**C**, **D**). Stroma and corneal endothelium observed under low magnification (**E**, **F**). Descemet's membrane observed under high magnification (**G**, **H**). Corneal endothelium observed under high magnification (**I**, **J**). No significant differences were found between the 8-week-old *Hspg2*$^{-/-}$-Tg mice and WT mice in regard to the construction of the stroma and endothelium. K, keratocytes; St, stroma; Des, Descemet's membrane; End, endothelium. Scale bar: (**A**, **B**) 2 μm; (**C**, **D**, **I**, **J**) 0.5 μm; (**E**, **F**) 5 μm; (**G**, **H**) 1 μm.

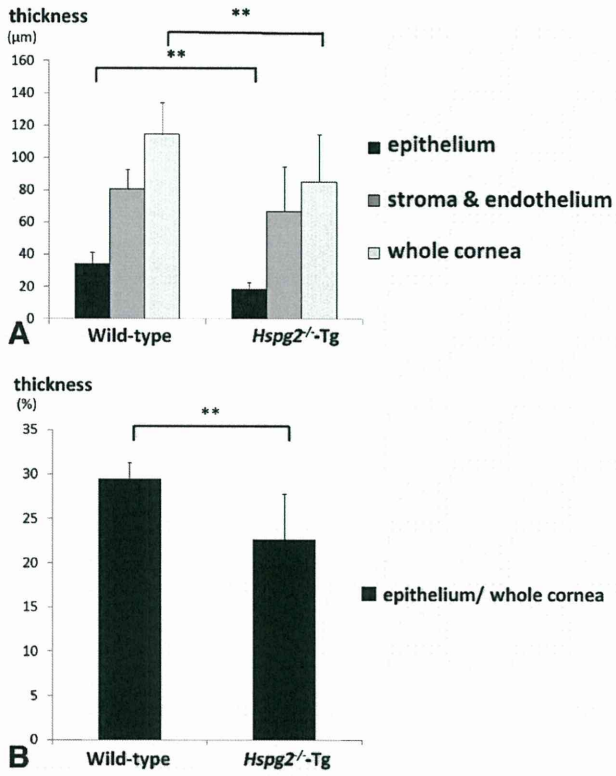

FIGURE 4. Morphometry of corneal thickness. Comparison of central corneal thickness. (**A**) The central corneal epithelial cell layer of the 8-week-old *Hspg2*$^{-/-}$-Tg mice was significantly thinner than that of the 8-week-old WT mice ($n = 6$; $P = 0.0022$). The full central corneal thickness was significantly thinner in the 8-week-old *Hspg2*$^{-/-}$-Tg mice compared with that in the 8-week-old WT mice ($n = 6$; $P = 0.0411$). Comparison of the ratio of the epithelial cell layer thickness to the full corneal thickness measured at the central cornea (**B**). The ratio of epithelial cell layer thickness to full corneal thickness was significantly lower in the *Hspg2*$^{-/-}$-Tg mice than in the WT mice ($n = 6$; $P = 0.0043$; Mann-Whitney U test: $^{*}P < 0.05$, $^{**}P < 0.01$, $^{***}P < 0.0001$).

both the *Hspg2*$^{-/-}$-Tg and WT epithelium (Fig. 5E), and there was no increase in RNA levels of active caspase3 of the apoptosis marker in both *Hspg2*$^{-/-}$-Tg and WT corneal epithelium (Fig. 5F), thus indicating that the loss of perlecan did not lead to a significant change in the rate of apoptosis. Therefore, the likely cause of the thinning of the 8-week-old *Hspg2*$^{-/-}$-Tg corneal epithelium was determined to be reduced cell proliferation.

Effect of Perlecan Deficiency on the Expression of Markers of Corneal Epithelial Differentiation

The expression of cytokeratin12 (K12), a corneal differentiation marker, in the 8-week-old *Hspg2*$^{-/-}$-Tg mice was significantly decreased compared with that in the WT mice examined by immunohistochemistry (Figs. 6A1, A2). Real-time PCR for K12 in the *Hspg2*$^{-/-}$-Tg epithelium showed a 54% decrease in RNA levels compared with the WT epithelium ($n = 5$; $P = 0.4698$; Fig. 6E). Connexin43 (Cx43), a gap junction protein, was found to be present in the corneal basal cell layers in the WT epithelium, but was absent in the *Hspg2*$^{-/-}$-Tg epithelium by immunohistochemistry (Figs. 6B1, 6B2). Real-time PCR for Cx43 in the *Hspg2*$^{-/-}$-Tg epithelium showed a 41% decrease in RNA levels compared with that in the WT epithelium ($n = 5$; $P = 0.4698$; Fig. 6E). The expression of Notch1 in the *Hspg2*$^{-/-}$-Tg corneal epithelium was significantly decreased compared with that of the WT epithelium by immunohistochemistry (Figs. 6C1, 6C2). Real-time PCR showed that the *Hspg2*$^{-/-}$-Tg mutation caused a significantly decrease in Notch1 RNA levels in the corneal epithelium, compared with that in the WT mice ($n = 5$; $P = 0.0159$; Fig. 6E). The expression of Pax6, a developmental regulator marker, was shown by immunohistochemistry to be significantly decreased in the corneal epithelium in the *Hspg2*$^{-/-}$-Tg mice compared with that of the WT mice (Figs. 6D1, 6D2). Real-time PCR for Pax6 in the *Hspg2*$^{-/-}$-Tg epithelium showed a significant decrease in RNA levels compared with that in the WT epithelium ($n = 5$; $P = 0.0159$; Fig. 6E).

DISCUSSION

In this study, perlecan was identified in corneal epithelial BM and the epithelium was shown to be thin and poorly differentiated in perlecan-deficient mice (*Hspg2*$^{-/-}$-Tg) and accompanied by the downregulation of Ki67, K12, Cx43, Notch1, and Pax6. However, the gross morphology of the corneal epithelium was not retarded in the *Hspg2*$^{-/-}$-Tg mice, suggesting that perlecan is not critically necessary in this process. Therefore, perlecan may be essential for the structure but not the development of corneal epithelium. In normal corneal epithelium, epithelial cells in the last phase of their differentiation undergo apoptosis as they reach the superficial cell layer. Since the cell death rate of the corneal epithelial cells in the *Hspg2*$^{-/-}$-Tg mice was similar to that in WT mice, the failure of those cells to form multilayered corneal epithelium must be due to the apparent decrease in the proliferation and differentiation rates in corneal epithelial cells. In this present study, we revealed that the expression of Ki67, K12, Cx43, Notch 1, and Pax6, which are markers of cell proliferation and differentiation, was reduced in the *Hspg2*$^{-/-}$-Tg mice, compared with that of the WT mice. Therefore, our findings revealed that perlecan in the BM of corneal epithelium may be critical for normal epithelial formation and terminal differentiation.

It has been reported that K12 is essential for the differentiation and maintenance of corneal epithelium integrity.,[18,19] Targeted deletion of K12 in a mouse model showed fewer cellular layers in the corneal epithelium and corneal fragility.[19] The findings of this study showed that downregulation of the expression of K12 at protein and RNA levels may be one of the causes of aberrant differentiation in the *Hspg2*$^{-/-}$-Tg corneal epithelium. From another aspect, it has been reported that the gap junction marker Cx43 mediates the intercellular diffusion ions and other small molecules,[20–22] thereby contributing to the regulation of tissue differentiation and homeostasis.[23] Of particular interest, the expression of Cx43 was noted in the corneal epithelial basal cells in the WT corneal epithelium, but not in the *Hspg2*$^{-/-}$-Tg epithelium, thus suggesting that the basal cell environment is impaired by gap junction functional decline. Therefore, the downregulation of Cx43 in the *Hspg2*$^{-/-}$-Tg mice most likely impairs the differentiation and structure of the corneal epithelium.

It has been reported that the Notch signaling pathway, another corneal homeostasis marker, limits cell proliferation and promotes differentiation.[24–27] In this study, the expression of Notch1 was decreased in the *Hspg2*$^{-/-}$-Tg mice, compared with that in the WT mice. Recently, Vauclair et al.[27] demonstrated that Notch1-deficient corneal cells lose their ability to heal and repair wounded corneal epithelium. The findings of that study showed that instead of generating new corneal epithelium after injury, those cells repair the wound by forming a hyperproliferative epidermislike epithelium. This process involves the secretion of FGF-2 through Notch1 signaling in the epithelium.[27] It is well known that FGF-2 is a growth factor of corneal epithelial cells.[28,29] Loss of Notch 1 in the corneal

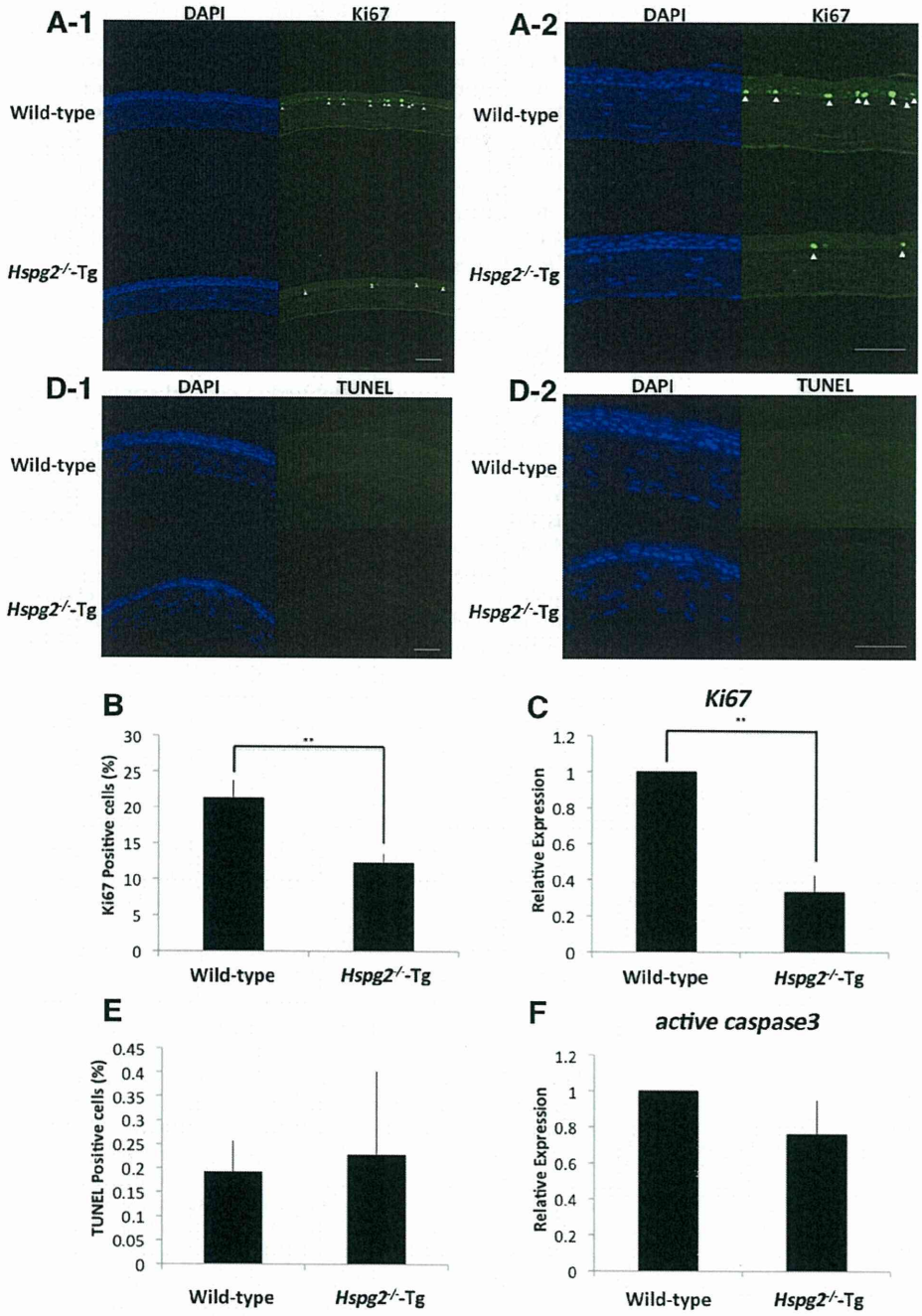

FIGURE 5. Proliferation and cell death in the *Hspg2*$^{-/-}$-Tg corneal epithelium. Immunohistochemistry showed a decreased number of cells containing Ki67 (Alexa488, *green*, *white arrow*) in the 8-week-old *Hspg2*$^{-/-}$-Tg versus WT corneal epithelium (DAPI, *blue*; **A1**, **A2**). The percentage of Ki67-positive cells in the corneal epithelium showed a 9.0% decrease in the *Hspg2*$^{-/-}$-Tg mice (±SEM, $n = 6$, $P = 0.0087$; **B**). Quantification of RNA levels for Ki67 in the corneal epithelium (±SEM; $n = 5$; $P = 0.0159$; **C**). In the superficial corneal cells, there was almost no TUNEL-positive staining (**D1**, **D2**). The percentage of TUNEL-positive cells in the corneal epithelium (±SEM, $n = 6$; **E**). Quantification of RNA levels for active caspase3 in the corneal epithelium (±SEM; $n = 5$; **F**; Mann-Whitney U test: $^{*}P < 0.05$, $^{**}P < 0.01$, $^{***}P < 0.0001$). Scale bar: 50 μm. Low magnification: **A1**, **D1**; high magnification: **A2**, **D2**.

epithelium resulted first in upregulation of FGF-2 by the corneal epithelium, suggesting that Notch1 signaling repressed its expression.[27] Despite the decreased expression of Notch1, a hyperproliferative change of corneal epithelium was not observed in the *Hspg2*$^{-/-}$-Tg mice. Since FGF-2 is a ligand of perlecan, there may be a possibility that a high dose of FGF-2 could not be maintained in the BM of the corneal epithelium of *Hspg2*$^{-/-}$-Tg mice.[30–35] Reportedly, FGF-7 is also a ligand of perlecan.[1] In a recent study, Lovicu et al.[36] showed hyperproliferation of embryonic corneal epithelial cells in transgenic mice engineered to overexpress human FGF-7 in the eye. Chikama et al.[37] analyzed the effects of excess FGF-7 on both the proliferation and differentiation of corneal epithelium in an FGF-7 transgenic mouse model in which cornea-specific FGF-7 was overexpressed. In that study, the mice exhibited epithelial hyperplasia, accompanied by the downregulation of K12. According to these results, the mechanism of the poor differentiation of the epithelium in *Hspg2*$^{-/-}$-Tg mice is due to the lack of the FGF-2 or FGF-7 that links to perlecan in the BM. Therefore, the strong correlation between the presence of perlecan in the BM and the formation of normal corneal epithelium suggests that perlecan functions as a reservoir for soluble factors involved in the proliferation and differentiation of corneal epithelial cells.

It should be noted that the *Hspg2*$^{-/-}$-Tg mice had microphthalmos. This condition has been reported in Pax6-deficient mice.[38–41] These reports suggest that Pax6 is a key developmental regulator and that it is generally essential for morphogenesis in the eye. Pax6 has autonomous roles in all eye tissues, where it is expressed at several developmental stages. Re-

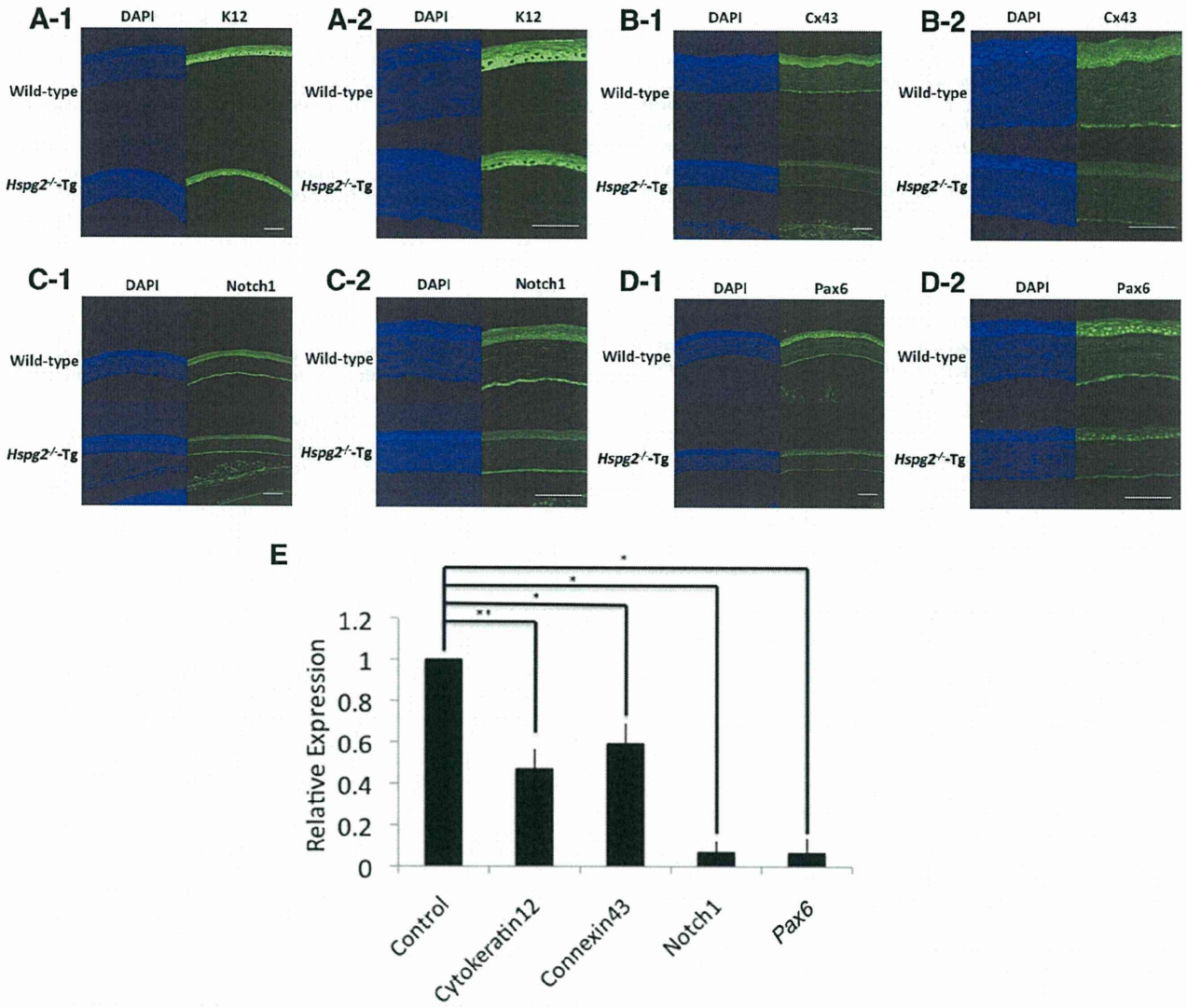

Figure 6. Expression of differentiation and developmental regulator markers in the 8-week-old *Hspg2*$^{-/-}$-Tg corneal epithelium demonstrated that the expression of cytokeratin12 (K12) in the *Hspg2*$^{-/-}$-Tg epithelium was significantly decreased compared with that in the WT epithelium (**A1**, **A2**). *Hspg2*$^{-/-}$-Tg corneal epithelium showed no expression of Connexin43 (Cx43; **B1**, **B2**). The expression of Notch1 in *Hspg2*$^{-/-}$-Tg corneal epithelium was significantly decreased compared with that in the WT epithelium (**C1**, **C2**). *Hspg2*$^{-/-}$-Tg corneal epithelium showed decreased Pax6 expression compared with that in the WT epithelium (**D1**, **D2**). Quantification of RNA levels for differentiation and developmental regulator markers in corneal epithelium (±SEM, $n = 5$; **E**; Mann-Whitney U test: $^{*}P < 0.05$, $^{**}P < 0.01$, $^{***}P < 0.0001$). Scale bar: 50 μm. Low magnification: **A1**, **B1**, **C1**, **D1**; high magnification: **A2**, **B2**, **C2**, **D2**.

cently, a report by Garcia-Villegas et al.[42] revealed that Pax6 is the earlier differentiation marker expressed by corneal epithelial cells and that it is the main driver of the differentiation of corneal epithelial cells, as the expression of Pax6 promotes the differentiation of corneal epithelial cells. On the other hand, transgenic mice overexpressing Pax6 in the corneal epithelium also showed abnormal epithelial cell morphology. These results indicate that a correct Pax6 dosage for the normal development of corneal epithelium may be important. In this present study, we demonstrated that the corneal epithelium of *Hspg2*$^{-/-}$-Tg mice was thinner and not well differentiated and that the phenotypes became more severe with age. The corneal epithelial phenotype was similar to that of Pax6-deficient mice. Thus, the downregulation of Pax6 in the corneal epithelium of *Hspg2*$^{-/-}$-Tg mice is likely to be a factor in the observed microphthalmos and thinner epithelium. We theorize that the downregulation of K12, Cx43, Notch1, and Pax6 probably occurs to prevent the proliferation and the differentiation from basal cells to wing cells, thus making the corneal epithelium of *Hspg2*$^{-/-}$-Tg mice thinner than that of WT mice with downregulation of the expression of Ki67.

In summary, by using perlecan-deficient mice (*Hspg2*$^{-/-}$-Tg) we demonstrated for the first time that perlecan is essential for the structure of corneal epithelium, as it controls the expression of markers for the proliferation or differentiation of corneal epithelial cells. Our findings revealed that perlecan in the BM of corneal epithelium were critical for normal epithelial structure and terminal differentiation.

Acknowledgments

The authors thank Glenn Longenecker and Ashok B. Kulkarni for help in creating the mutant mice, Yoshihiko Yamada for critical reading of the manuscript, and Saori Ito for secretarial assistance.

References

1. Knox SM, Whitelock JM. Perlecan: how does one molecule do so many things? *Cell Mol Life Sci.* 2006;63:2435-2445.
2. Murdoch AD, Dodge GR, Cohen I, Tuan RS, Iozzo RV. Primary structure of the human heparin sulfate proteoglycan from basement membrane (HSPG2/perlecan): a chimeric molecule with multiple domains homologous to the low density lipoprotein receptor, laminin, neural cell adhesion molecules, and epidermal growth factor. *J Biol Chem.* 1992;267:8544-8557.
3. Noonan DM, Fulle A, Valente P, et al. The complete sequence of perlecan, a basement membrane heparan sulfate proteoglycan, reveals extensive similarity with laminin A chain, low density lipoprotein-receptor, and the neural cell adhesion molecule. *J Biol Chem.* 1991;26:22939-22947.
4. Hassell JR, Robey PG, Barrach HJ, et al. Isolation of a heparan sulfate-containing proteoglycan from basement membrane. *Proc Natl Acad Sci USA.* 1980;77:4494-4498.
5. Iozzo RV. Perlecan: a gem of a proteoglycan. *Matrix Biol.* 1994; 14:203-208.
6. Iozzo RV. Basement membrane proteoglycans: from cellar to ceiling. *Nat Rev Mol Cell Biol.* 2005;6:646-656.
7. Whitelock JM, Iozzo RV. Heparan sulfate: a complex polymer charged with biological activity. *Chem Rev.* 2005;105:2745-2764.
8. Handler M, Yurchenco PD, Iozzo RV. Developmental expression of perlecan during murine embryogenesis. *Dev Dyn.* 1997;210:130-145.
9. Knox S, Melrose J, Whitelock J. Electrophoretic, biosensor, and bioactivity analyses of perlecans of different cellular origins. *Proteomics.* 2001;1:1534-1541.
10. Jiang X, Couchman JR. Perlecan and tumor angiogenesis. *J Histochem Cytochem.* 2003;51:1393-1410.
11. Zhou Z, Wang J, Cao R, et al. Impaired angiogenesis, delayed wound healing and retarded tumor growth in perlecan heparan sulfate-deficient mice. *Cancer Res.* 2004;64:4699-4702.
12. Arikawa-Hirasawa E, Watanabe H, Takami H, Hassell JR, Yamada Y. Perlecan is essential for cartilage and cephalic development. *Nat Genet.* 1999;23:354-358.
13. Xu Z, Ichikawa N, Kosaki K, et al. Perlecan deficiency causes muscle hypertrophy, a decrease in myostatin expression, and changes in muscle fiber composition. *Matrix Biol.* 2010;29:461-470.
14. Rossi M, Morita H, Sormunen R, et al. Heparan sulfate chains of perlecan are indispensable in the lens capsule but not in the kidney. *EMBO J.* 2003;22:236-245.
15. Sher I, Zisman-Rozen S, Eliahu L, et al. Targeting perlecan in human keratinocytes reveals novel roles for perlecan in epidermal formation. *J Biol Chem.* 2006;281:5178-5187.
16. Kabosova A, Azar DT, Bannikov GA, et al. Compositional differences between infant and adult human corneal basement membranes. *Invest Ophthalmol Vis Sci.* 2007;48:4989-4999.
17. Costell M, Gustafsson E, Aszódi A, et al. Perlecan maintains the integrity of cartilage and some basement membranes. *J Cell Biol.* 1999;147:1109-1122.
18. Chaloin-Dufau C, Sun TT, Dhouailly D. Appearance of the keratin pair K3/K12 during embryonic and adult corneal epithelial differentiation in the chick and in the rabbit. *Cell Differ Dev.* 1990;32: 97-108.
19. Kao WW, Liu CY, Converse RL, et al. Keratin 12-deficient mice have fragile corneal epithelia. *Invest Ophthalmol Vis Sci.* 1996;37: 2572-2584.
20. Kimura K, Teranishi S, Nishida T. Establishment of human corneal epithelial cells stably expressing human connexin43. *Exp Eye Res.* 2010;90:4-9.
21. Ko JA, Yanai R, Morishige N, Takezawa T, Nishida T. Upregulation of connexin43 expression in corneal fibroblasts by corneal epithelial cells. *Invest Ophthalmol Vis Sci.* 2009;50:2054-2060.
22. Yang HS, Lu XH, Chen DY, et al. Upregulated expression of connexin43 in spinal ligament fibroblasts derived from patients presenting ossification of the posterior longitudinal ligament. *Spine* (Phila Pa 1976). 2011;36:2267-74.
23. Kumar NM, Gilula NB. The gap junction communication channel. *Cell.* 1996;84:381-388.
24. Ma A, Boulton M, Zhao B, Connon C, Cai J, Albon J. A role for notch signaling in human corneal epithelial cell differentiation and proliferation. *Invest Ophthalmol Vis Sci.* 2007;48:3576-3585.
25. Djalilian AR, Namavari A, Ito A, et al. Down-regulation of Notch signaling during corneal epithelial proliferation. *Mol Vis.* 2008;14: 1041-1049.
26. Thomas PB, Liu YH, Zhuang FF, et al. Identification of Notch-1 expression in the limbal basal epithelium. *Mol Vis.* 2007;13:337-344.
27. Vauclair S, Majo F, Durham AD, et al. Corneal epithelial cell fate is maintained during repair by Notch1 signaling via the regulation of vitamin A metabolism. *Dev Cell.* 2007;13:242-253.
28. Hu C, Ding Y, Chen J, et al. Basic fibroblast growth factor stimulates epithelial cell growth and epithelial wound healing in canine corneas. *Vet Ophthalmol.* 2009;12:170-175.
29. Wang X, Zhou X, Ma J, et al. Effects of keratinocyte growth factor-2 on corneal epithelial wound healing in a rabbit model of carbon dioxide laser injury. *Biol Pharm Bull.* 2010;33:971-976.
30. Friesel RE, Maciag T. Molecular mechanisms of angiogenesis: fibroblast growth factor signal transduction. *FASEB J.* 1995;9:919-925.
31. Takehara K. Growth regulation of skin fibroblasts. *J Dermatol Sci.* 2000;24(suppl 1):S70-S77.
32. Aviezer D, Hecht D, Safran M, et al. Perlecan, basal lamina proteoglycan, promotes basic fibroblast growth factor-receptor binding, mitogenesis, and angiogenesis. *Cell.* 1994;79:1005-1013.
33. Knox S, Merry C, Stringer S, Melrose J, Whitelock J. Not all perlecans are created equal: interactions with fibroblast growth factor (FGF) 2 and FGF receptors. *J Biol Chem.* 2002;277:14657-14665.
34. Whitelock JM, Murdoch AD, Iozzo RV, Underwood PA. The degradation of human endothelial cell-derived perlecan and release of bound basic fibroblast growth factor by stromelysin, collagenase, plasmin, and heparanases. *J Biol Chem.* 1996;271:10079-10086.
35. Whitelock JM, Graham LD, Melrose J, et al. Human perlecan immunopurified from different endothelial cell sources has different adhesive properties for vascular cells. *Matrix Biol.* 1999;18: 163-178.
36. Lovicu FJ, Kao WW, Overbeek PA. Ectopic gland induction by lens-specific expression of keratinocyte growth factor (FGF-7) in transgenic mice. *Mech Dev.* 1999;88:43-53.
37. Chikama T, Liu CY, Meij JT, et al. Excess FGF-7 in corneal epithelium causes corneal intraepithelial neoplasia in young mice and epithelium hyperplasia in adult mice. *Am J Pathol.* 2008;172:638-649.
38. Chanas SA, Collinson JM, Ramaesh T, et al. Effects of elevated Pax6 expression and genetic background on mouse eye development. *Invest Ophthalmol Vis Sci.* 2009;50:4045-4059.
39. Favor J, Bradley A, Conte N, et al. Analysis of Pax6 contiguous gene deletions in the mouse, Mus musculus, identifies regions distinct from Pax6 responsible for extreme small-eye and belly-spotting phenotypes. *Genetics.* 2009;182:1077-1088.
40. Shaham O, Smith AN, Robinson ML, et al. Pax6 is essential for lens fiber cell differentiation. *Development.* 2009;136:2567-2578.
41. Wolf LV, Yang Y, Wang J, et al. Identification of pax6-dependent gene regulatory networks in the mouse lens. *PLoS One.* 2009;4: e4159.
42. García-Villegas R, Escamilla J, Sánchez-Guzmán E, et al. Pax-6 is expressed early in the differentiation of a corneal epithelial model system. *J Cell Physiol.* 2009;220:348-356.

Journal of Math-for-Industry, Vol. 3 (2011A-8), pp. 79–88

Math-for-industry
Education & Research Hub

Dynamic mathematical modeling of cell-fractone interactions

Monique Chyba, Frederic Mercier, John Rader, Vanessa Douet, Eri Arikawa-Hirasawa, Youngsu Chow Kwon and Rich Kodama

Received on February 19, 2011

Abstract. Within the last 20 years, new biological structures called *fractones*, named in honor of the late Dr. Benoit Mandelbrot due to their fractal-like appearance, have been discovered by cell biologists. Their primary purposes are theorized to pertain to the major processes of the life cycle of cells, namely cell division, migration, and differentiation. Building on the back of the discretized diffusion equations, we built a mathematical model of how these fractones interact with the cells and the associated growth factors produced in order to gain insight into the growth process as a whole. As it is shown in this paper, the complexity of this biological process opens the door to entirely new questions in the field of control theory.

Keywords. Morphogenesis, Fractones, Control Theory, Computational Modeling.

1. Introduction

The primary goal of this paper is, motivated by the hypothesis that new biological structures named fractones pertain to the major process of the life cycle, to formulate questions in the field of control theory for a new category of systems.

Neurulation and subsequent events of brain's formation involve multiple neurogenic growth factors that in turn induce neuroepithelial cell proliferation, differentiation and migration. From the distribution and activation of these growth factors in space and time will depend the morphogenic events of the developing mamalian brain. The distribution and activation of those growth factors in space and time will depend the morphogenic events of the developing mamalian brain. However, the process organizing the distribution/availability of growth factors within the neuroepithelium is not understood. It is known that extracellular matrix (ECM) molecules such as heparan sulfate proteoglycans (HSPG) interact and strongly influence growth factors in the extracellular space prior to the recognition of growth factors by cell surface receptors and subsequent biological activation. The HSPG capture, concentrate and protect growth factors in specialized locations [1, 7, 17, 26]. For numerous heparin-binding growth factors such as fibroblast growth factors (FGF) and bone morphogenetic protein (BMP), very active families of growth factors for developmental neurogenesis, HSPG are even thought to be obligatory for presenting the growth factors to the cell surface receptors of the target cells [1, 2, 15, 26]. Therefore, the ECM may play a crucial role as a topological organizer of growth factor capture and activation, and as a potential driver of morphogenic events. We have characterized novel ECM structures, termed fractones, that directly contact neural stem and progenitor cells in the adult brain neurogenic zone [10, 13, 14]. Adult fractones are highly immunoreactive for HPSG, capture and concentrate FGF-2 [10] and BMP-7 [6] and are associated with cell proliferation in the neurogenic zone [10]. In addition, we have recently shown that FGF-2 and BMP-7 must bind fractones in the neural stem cell niche to regulate neural stem cell proliferation and the production of new neural cells in adulthood [6]. Our preliminary results indicate the presence of fractones (laminin and HSPG immunoreactive punctae) associated with neuroepithelial cell proliferation during development, capable of capturing FGF-2, and similar to laminin immunoreactive punctae characterized by others during development [11, 12, 20]. Therefore, "embryonic fractones" are good candidates to collect and promote growth factors at the surface of the neuroepitelial cells to spatially control their proliferation. Our hypothesis is that fractones are the captors that spatially control the activation of growth factors in a precise location to generate a morphogenic event.

To validate this hypothesis, we propose to develop and analyze a mathematical model predicting cell proliferation from the spatial distribution of fractones in a developing mouse. Dynamic mathematical modeling, i.e. models that represents change in rates over time, serves several purposes [8]. Using computer simulations, by mimicking the assumed forces resulting in a system behavior, the dynamic model helps us to understand the nonlinear dynamic of the system under study. Such approach is especially well suited for biological systems whose complexity renders a purely analytical approach unrealistic. Moreover, it allows us to overcome the excessively demanding purely experimental

approach to understand a biological system. Our primary goal in this paper is to develop a model that contains the crucial features of our hypothesis and at the same time that is sufficiently simple to allow an understanding of the underlying principles of the observed system.

We propose to model this biological process as a control system, the control depicting the spatial distribution of the active fractones. This is a novel approach with respect to the most commonly reaction-diffusion models seen in the literature on morphogenesis, however it is not that surprising. Indeed, control theory is instrumental to overcome many challenges faced by scientists to design systems with a very high degree of complexity and interaction with the environment [4, 5, 16]. Examples of its applicability in physical and biological systems are numerous [18, 19]. In this paper, we will highlight the fact that due to the specific nature of morphogenesis and in particular of the cell's proliferation, our innovative model opens an entirely new area in control theory. The reason comes from the fact that in this proposal the state space of our control system is dynamic; this is an intrinsic property of biological systems. In physics, for instance, the state space is static and the equations of motion are derived from minimizing a Lagrangian. In engineering, the configuration manifold is fixed and, one either attempts to determine the evolution of the system while minimizing a prescribed cost or one tries to design controls to take into account uncertainties of the system. As a result, new methods have to be proposed to analyze biological systems from the control theory point of view. This will advance the field of control theory by considering new problems and by providing insight toward the development of innovative ideas and methods to solve these types of problems. In this paper, we take a first step in that direction.

2. Background

2.1. Neurulation

A fundamental problem is to understand how growth factors control the topology of cell proliferation and direct the construction of the forming neural tissue. It has been demonstrated that ECM molecules, particularly proteoglycans, strongly influence growth factor-mediated cell proliferation. ECM proteoglycans can capture and present growth factors to the cell surface receptors to ultimately trigger the biological response of growth factors.

F. Mercier and his collaborators have discovered ECM structures that are associated with proliferating cells in the stem cell niche of the adult mammalian brain [13, 14, 10]. These structures, termed fractones, display a complex branched morphology by transmission electron microscopy [13, 14] but appear as small punctae by immunofluorescence microscopy after immunolabeling for laminin, collagen IV or heparan sulfate proteoglycans (HSPG) [13, 10]. Fractones hold a high potential as captors of mitotic and neurogenic growth factors via their HSPG [10]. The most recent results indicate that fibroblast growth factor-2 (FGF-2) and bone morphogenetic factor-7 (BMP-7) must bind fractones to respectively stimulate and inhibit cell proliferation in the adult neurogenic niche [6]. Do fractones exist during development? Several authors demonstrated the occurence of laminin immunoreactive punctae during development [12, 23, 24]. However, the function of these punctae during development has not been reported. F. Mercier investigated the presence of these punctae at several stages of mouse development, and their potential as captors of FGF-2 (personal communication).

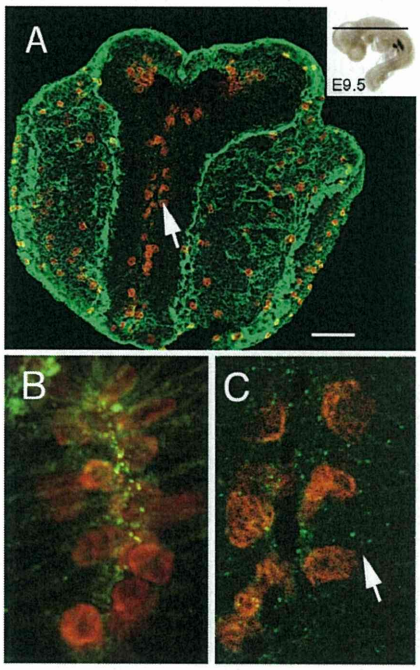

Figure 1: **Characterization of fractones in the mouse neuroepithelium during brain morphogenesis.** *A. Laser scanning confocal microscopy image showing the section of the whole head of an E9.5 embryo (9.5 days post-coitum). Proliferating neuroepithelial cells were visualized by phosphorylated histone-3 (PH3, a marker of mitosis) immunofluorescence cytochemistry (red). The extracellular matrix material was revealed by immunoreactivity for laminin, a ubiquitous glycoprotein found in basement membranes and fractones. However, fractones are too small to be visualized at this level of magnification. Note that cells proliferate near the lumen of the forming cavity (arrow, neural groove). The plan of section is indicated in the inset. B. High magnification confocal microscopy field showing proliferating neuroepithelial cells (PH3 immunoreactivity, red) associated with fractone (green punctae) at E8.5. C. Magnification of the area indicated by an arrow in A showing that neuroepithelial cells also proliferate (red) next to fractones (green punctae, arrow) at E9.5. Scale bars. A: 50 m; B and C: 10 m.*

2.2. Control Theory

The history of mathematics used to solve problems arising from biology dates back several hundred years to the times of Bernoulli and Euler. Prior to the mid 1900s, though, biology served primarily as the inspiration to understanding larger problems rather than as a practical field to be studied under the rigors of applied mathematics. Many problems in the field, even simplified with strong assumptions and in their least-complex forms, were unable to be solved using traditional techniques of mathematicians due to their complexity. Within the last thirty years, and mostly due to the advent of the computer, researchers are now analyzing complex systems without unnecessary simplifications. With the capability to undertake more and more complex systems came a new era for mathematical and computational biology.

The appearance and usage of control theory in the field of biology is a relatively new idea, dating back only a few decades. The first real evidence of the usage of control theory to understand a biological process originates with Norbert Wiener [25], who developed many of the ideas of feedback and filtering in the early 1940s in collaboration with the Harvard physiologist Arturo Rosenblueth, who was, in turn, heavily influenced by the work of his colleague Walter Cannon [3], who coined the term homeostasis in 1932 to refer to feedback mechanisms for set-point regulation in living organisms. Rudolf Kalman [9] often used biological analogies in his discussion of control systems theory, and so did many other early researchers. Modern biological control, enveloped in the more general field of systems biology, eminates from the work of Ludwig von Bertalanffy[22] with his general systems theory. Born even more recently, the field of systems biology (the merging of biology, physics, engineering, and/or mathematics) is large and encompassing, so much so that it, at times, is hard to define what is and is not part of the field. Among the problems addressed by the field are: complex molecular systems; quantitative modeling of enzyme kinetics; mathematical modeling of population growth; simulations developed to study neurophysiology; control theory and cybernetics. Some recent problems approached by those studying control theory in the field of biology have been to model, among others: internal workings of the cells; molecular signaling or energy transfer (among RNA, DNA, proteins, etc.); cell signal transduction processes; neural pathways; regulation versus homeostasis; RNA/DNA transcription with an emphasis on mutation; and gene function and interactions. The breadth and variety of problems that can be modeled using control theory runs the gamut, from the molecular through the microscopic up to the macroscopic.

Many areas of biology have been affected by many areas of mathematical science, and the challenges of biology have also prompted advances of importance to the mathematical sciences themselves. The rapidly developing field of systems biology is tremendously exciting, and full of unique research opportunities and challenges, especially for the application of control theory.

Mathematically, the classical models attempting to describe morphogenesis are based on reaction-diffusion equations with the pioneering work of Turing [21]. Growth factors—then called chemicals—were allowed to freely and continually diffuse in the intracellular space. Reaction would occur in this soup of chemicals and those events would induce the cell to divide. Although Turing made a great attempt to mathematically portray morphogenesis, it is not an adequate model to describe the system given new discoveries and developments since the 1950s. Indeed, with his model Turing was describing how reactive chemicals produced in a static, living structure interact in a continuous medium (and, surprisngly, form wave-like patterns). Clearly, reaction-diffusion equations cannot be used to study the mechanisms of morphogenesis during development. Morphogenesis involves the capture and activation of growth factors by fractones at specific locations according to a precise timing. Moreover, the distribution of fractones is constantly changing during development, reflecting the dynamic of the morphogenic events. Therefore, the organizing role of fractones in morphogenesis must be analyzed by alternative mathematical models.

3. Mathematical Model

For the preliminary stages of our study we will provide only an approximate model of brain development. Additional parameters reflecting the neurulation process such as production of growth factors in precise locations will be incorporated later on. Let us present here a two-dimensional model of the morphogenesis process based on the existence of fractones.

3.1. Configuration Space

The morphogenic event will start from an initial configuration of cells immerged in what we call the ambiant space. Growth factors diffuse within the ambiant space. The ambiant space is discretised with a precision to be chosen by the user (eventually it will be determined by the experimental biological maps).

Definition 1. We call a square of our discretisation a unit. In the sequel, each unit will be identified to an integer pair (i, j). The origin of the discretisation is choosen arbitrarily and will be identified to $(0, 0)$.

Assumption 1. In the following, we assume that the space between the cells account for 20% of the total space occupied by the cells. This is reflected in our discretisation by representing a cell as a square composed of 81 units (i.e. a 9 by 9 square), while the "in-between cells" space is represented by single unit-rows and unit-columns. Notice that at this stage of the work it is an arbitrary choice and it will be straighforward to adjust it to reflect the observations from the experimental maps. Finally, in our discretisation, a fractone is represented as one unit, and will always be represented in green. In Figure 2, we represent two such discretisations for two different configurations of cells.

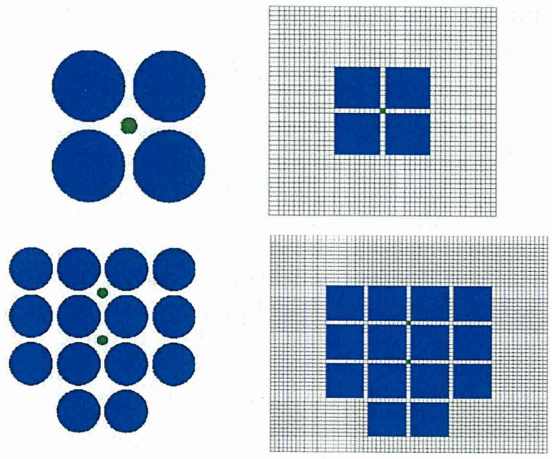

Figure 2: **Discretisation of given configurations of cells.** *The fractones are in green.*

The diffusion of growth factors occurs in the extra-cellular space around the cells as well as in the reminder of the ambiant space not filled with cells. Where a cell exists, the diffusion of growth factor is prevented since the cell acts like a wall. In our representation each new forming cell can be seen as the formation of a new obstacle in the ambiant space.

Assumption 2. In this paper, for simplicity we assume that the boundary of the ambiant space in which the biological process takes place is fixed but our definitions allow for boundaries that vary with time as well. Moreover, as a first step we assume the cells to be vertically and horizontally aligned.

Definition 2. At each time t of the biological process, we define the current configuration of cells associated with the remainder of the ambiant space as the Configuration Space of our system. By construction, in our case the configuration space is a topological space with holes (the cells), and will be denoted by $Conf(t)$.

Remark 1. Due to the morphogenic nature of the biological process under study, the configuration space is constantly evolving. This distinguishes in a very non trivial way our problem for the traditional problems in engineering or physics whose systems are usually defined on a static configuration space.

Prior to introducing the model, let us describe more precisely $Conf(t)$. To the discretisation of the initial configuration of cells and the ambiant space, i.e. $Conf(0)$, we associate a collection of indices $(i,j) \in I_0 \times J_0$ where each index is represented by an integer. Each pair of indexes represent a unit of our discretisation. For instance in Figure 2, the upper left configuration of cells assumed to be in squared ambiant space is associated to $I_0 = J_0 = \{0,1,\cdots,44\}\backslash(\{13,\cdots,21\}\cup\{23,\cdots,31\})$. As mentioned before, since cells are constantly forming, the configuration space evolves constantly as well, however it will always be formed by the product of unions of subsets of $\mathbb{Z}$. We introduce $Conf(t) = I_t \times J_t \subset \mathbb{Z}\times\mathbb{Z}$, where I_t, J_t are both unions of finite subsets of $\mathbb{Z}$. Note that with this equality we identify the configuration to its discretisation and that will be the case in all that follows. Indeed there is a one-to-one correspondance between both.

In our proposed model, the morphogenic events will be governed by a control system defined on a state space. The state space differs from the configuration space as follows. The state space represents the concentration of growth factor in each unit of our discretisation of the configuration space.

Assumption 3. For simplicity, in this paper we assume the diffusion of a unique type of growth factor and equal sensitivity of the fractones with respect to that growth factor. However, our model will be developed such that expanding to several type of growth factors and fractone sensitivity can be added in a straightforward way.

Definition 3. To each unit (i,j), and at each time t we associate a concentration of growth factor that we denote by $X_{ij}(t)$. The rate of change in the concentration of growth factor is described using classical diffusion equations.

3.2. Diffusion of Growth Factors in $Conf(t)$

Assume at first that there is no cells, therefore the growth factors diffuse freely in the ambiant space. The pure dissipation is then described by:

$$\dot{X}(t) = F^0(X(t)) \tag{1}$$

where the component of $X(t)$ are given by $X_{ij}(t)$ which represents the quantity of growth factor in unit (i,j) at time t as described in definition 3, and assuming diffusion occurs between a unit (i,j) and its heigth-neighbors we have:

$$\dot{X}_{ij}(t) = \nu_X[\sum_{k,l=-1}^{1}(X_{i+k,j+l}(t) - X_{ij}(t))], \quad (i,j) \in I_0 \times J_0. \tag{2}$$

Here the parameter ν_X represents the diffusion parameter associate to the considered growth factor. Assume now that a cell forms in the ambiant space. The cell therefore becomes an obstacle to the diffusion process. Mathematically, rather than looking at a cell as an obstacle, we identify the cell to a hole in a topological space. The hole depicting the location of the cell insures that the diffusion of the growth factor takes place in the remainder of the ambiant space only. By doing so we do not have to perturbe the diffusion process, instead we continuously modify the topological space within which the diffusion process takes place.

Let us describe the new state space on which the diffusion process takes place. Assume the cell is centered at unit (a,b). This means that at the time t at which the cell formed, the configuration space $I_t \times J_t$ transforms into a new configuration space $\tilde{I}_t \times \tilde{J}_t = I_t \times J_t\backslash(\{a-4,\cdots,a+$

$4\}\times\{b-4,\cdots,b+4\}$). Notice that since several cells might be forming at the same time, the topological changes in the state space will reflect all the created holes. We then have:

$$\dot{X}_{ij}(t) = \nu_X[\sum_{\substack{k,l=-1 \\ (i+k,j+l)\in \tilde{I}_t\times\tilde{J}_t}}^{1} (X_{i+k,j+l}(t) - X_{ij}(t))], \tag{3}$$

for $(i,j) \in \tilde{I}_t \times \tilde{J}_t$.

3.3. Fractones as Controllers

The next step is to introduce the fractones into our model. As mentioned before, a fractone is represented as a one unit (i,j) of our discretisation.

Assumption 4. The assumption is that the fractones store the quantity of growth factors that they capture, and that this quantity becomes unavailable to the diffusion process.

In other terms, if a fractone is associate to a unit (i,j) there is perturbation to the diffusion process as follows. We introduce a control function $u(t) = (u_{ij}(t)) \in \{0,1\}^{I_t\times J_t}$ defined on a time interval $[0,T]$, with T representing the duration of the cascade of morphogenic events under study. When a fractone becomes active in unit (i,j) at time t, the component $u_{ij}(t)$ of the control is turned on to 1 while it is set to zero otherwise (i.e. no fractone is associated to unit (i,j) or is not yet into an active mode). Once active the fractone stores the current quantity of growth factors available in unit (i,j) and acts as a captor for the diffusion process. In other words, diffusion from the unit associated to an active fractone to its neighbords is prevented. To represent this perturbed-diffusion process we define a control system:

$$\dot{X}(t) = F^0(X(t)) + \sum_{(i,j)\in I_t\times J_t} F^{(i,j)}(X(t))u_{(i,j)}(t), \tag{4}$$

where $X(t)$ is the state variable and denotes the concentration of growth factor X in the discretized configuration space $I_t \times J_t$ at time t, the drift vector field F^0 is given by the right-hand side of (3) and represents the regular diffusion of growth factors taking place in the configuration space, and finally the control vector fields perturbes the regular diffusion to account for the possible prescence of an active fractone. More precisely, we have:

$$F_{ij}^{(i,j)}(X(t)) = \nu_X(\sum_{\substack{k,l=-1,(k,l)\neq(0,0) \\ (i+k,j+l)\in I_t\times J_t}}^{1} X_{i,j}(t)), \tag{5}$$

and

$$F_{i+k,j+l}^{(i,j)}(X(t)) = -\nu_X X_{ij}(t), \tag{6}$$

for $k,l \in \{-1,0,1\}$, $(i+k,j+l) \in I_t \times J_t$. In our notation, $F_{mn}^{(i,j)}$ represents the component mn of the vector field $F^{(i,j)}$. What we have done is to artificially hide for the diffusion process the value of the quantity of growth factor available in unit (i,j) in which a fractone is active. This implies that continuously, the neighboring units will diffuse to unit (i,j) and that the quantity of growth factor collected there is then stored over time and hidden for the diffusion process. Once the stored quantity reach a given threshold, mitosis can happen.

Definition 4. An admissible control is a mesureable function $u : [0,T] \to \{0,1\}^{n(t)}$ where T represents the duration of the morphogenic event under study, and $n(t)$ is the number of pairs included in $I_t \times J_t$.

3.4. Mitosis

The motivation behind the introduction of fractones as controllers comes from the hypothesis that it is the fractones that proceed with the order to the cell to undergo mitosis. Indeed, an active fractone stores quantity of growth factors through the diffusion process, and once this quantity reaches a prescribed threshold all the cells associated to this active fractone duplicate. In other words, the spatial distribution of fractones determines the morphogenic events.

To translate this mathematically, we can equivalently state that the spatial distribution of fractones and the diffusion process of growth factors regulate the appearance and the location of holes in our topological space, namely the configuration space. A natural question arises: when a cell undergoes mitosis, how does the existing mass of cells deform? At this stage, we will limit ourselves to simple assumptions to avoid to unnecessarily complexify the problem.

Based on assumption 2, in the sequel we identify a cell C to a unit of our discretisation. Indeed, since we assume our cells to be squares of 9×9 units of our discretisation and to be vertically and horizontally aligned, a cell C is completely determined by its middle unit (a,b). We write $C = (a,b)$. The following assumptions that regulate the deformation of the existing mass of cells once mitosis occurs is arbitrary and can be modified easily.

Assumption 5. Let unit (i,j) represent an active fractone. Associated to this fractone, there are at most four cells. The existing cells are represented by their central units $(i+\alpha 5, j+\alpha 5)$, $\alpha = \pm 1$. When the fractone (i,j) reaches the threshold value for the quantity of growth factor, all cells associated to the fractones are given the order to duplicate. Mathematically, it can be expressed as follows. If $(i+\alpha 5, j+\alpha 5) \in I_t \times J_t$, where $\alpha = \pm 1$, then the cell $(i+\alpha 5, j+\alpha 5)$ duplicates.

Assume cell (a,b) receives the order to duplicate. The next step is to model the deformation of the current configuration of cells or equivalently to define the location of a new hole in our topological space, namely the state space. First we introduce the following notion of distance.

Definition 5. Let $a = (a_1,a_2)$ and $b = (b_1,b_2)$ be two units such that $a_1 = b_1 \bmod 10$ and $a_2 = b_2 \bmod 10$. The linear distance between a and b is defined by $d_L(a,b) =$

$(|a_1 - b_1| + |a_2 - b_2|)$ and the geometric distance is defined by $d_G(a,b) = \sqrt{|a_1 - b_1|^2 + |a_2 - b_2|^2}$.

The geometric distance helps to determine a hierachy between units that are at the same linear distance from a given unit. This notion of geometric distance is based on the assumption that the mass of cell is optimizing its shape by prioritizing compactness. Clearly, we have that $d_G(a,b) = 10\sqrt{n^2+m^2}$ with $n, m \in \mathbb{Z}$. Notice that given unit (a,b), the closest units mod 10 from (a,b) are at a distance 1, and there are 4 of them. The next closest units are at a distance $\sqrt{2}$ and there are also 4 of them. The table below describes the possible distances, only one quandrant is displayed since it is symmetrical with respect to the other quadrants, and the table is symmetrical about its diagonal. The pattern is very clear. For the distances represented either by a number in the diagonal in Table 1 or by by an integer that is not issued from a Pythagorean triple, globally there are exactly 4 units at such distance mod 10 from unit (a,b). If the integer comes from a Pythagorean triple (such as 5) there are 12 such units and for any other number there are exactly 8 choices.

0	1	2	3	4	5	6
1	$\sqrt{2}$					
2	$\sqrt{5}$	$2\sqrt{2}$				
3	$\sqrt{10}$	$\sqrt{13}$	$3\sqrt{2}$			
4	$\sqrt{17}$	$2\sqrt{5}$	5	$4\sqrt{2}$		
5	$\sqrt{26}$	$\sqrt{29}$	$\sqrt{34}$	$\sqrt{41}$	$5\sqrt{2}$	
6	$\sqrt{37}$	$2\sqrt{10}$	$3\sqrt{5}$	$2\sqrt{13}$	$\sqrt{61}$	$6\sqrt{2}$

Table 1: Distance distribution for the deformation of the mass of cell as measured from the active fractone.

Let us describe our strategy in details. We identify the active fractone to unit (i,j). To this fractone there are at most 4 cells that are connected, those are described by $C_1 = (i+10, j-10), C_2 = (i-10, j-10), C_3 = (i-10, j+10)$ and $C_4 = (i+10, j+10)$. At time t, the active fractone (i,j) reaches the threshold for the configuration of growth factor. The connected cells then get the order to duplicate. The algorithm works as follows: first, it checks if $(i+5, j+5) \in I_t \times J_t$, if not there is a cell $C = (i+5, j+5)$, duplication takes place and the mass of cells deforms in the direction of the closest free space in terms of the geometric distance to contain a cell. Since there might be more than one such spot, we must make an arbitrary choice. Then, the algorithm checks for units in the first quadrant $(i+5)^+, (j+5)^-$ where $(i+5)^+$(resp. $(i+5)^-$)=set of indices k such that $k = (i+5)+\mathbb{N}$ (resp. $k = (i+5)-\mathbb{N}$) and $(j+5)^-$(resp. $(j+5)^+$)=set of indices l such that $l = (j+5) - \mathbb{N}$ (resp. $l = (j+5) + \mathbb{N}$). For a distance represented by mutliple units in this first quadrant, it will choose the one with the second index that is the closest to $j+5$. In case no unit are at the prescribed distance from $(i+5, j+5)$ mod 10, the algorithm does a similar search into the second quadrant $(i+5)^-, (j+5)^-$ and the units are considered clockwise starting from the first quandrant. If still no such units are found in the second quadrant, it then moves the search to the third quadrant $(i+5)^-, (j+5)^+$ and finally to the fourth quadrant $(i+5)^+, (j+5)^+$. Once this cycle is complete, the algorithm does the same calculations for a potential cell at $(i+5, j-5)$ associated to the active fractone, to be followed by the same two cycles for $(i-5, j-5)$ and $(i-5, j+5)$.

4. Statement of the Problem

This section is the main objective of the paper now that we have described mathematically the important structures of our study we can state the problem in a formal way.

To summarize what was done in the previous sections, the morphogenic events have been modeled as an affine control system of the form:

$$\dot{x}(t) = F^0(x(t)) + \sum_{i=1}^{n} u_i(t) F^i(x(t)), x(t) \in M(t) \tag{7}$$

where the state space $M(t)$ varies with time, $\dim M(t) = n(t)$, and such that $u(t)$ is an admissible control. In other words, it is a fully actuated system defined on a dynamical state space. Notice that the dimension of $M(t)$ is arbitrary since it depends on our discretisation, but the important feature of our system is that this dimension varies with respect to time. The problem is now the following:

Problem. *Given an initial and final configuration of cells in a prescribed ambiant space, determine an initial concentration of growth factors and a dynamic spatial distribution of fractones such that the mass of cells transforms from its initial configuration to its final configuration.*

An initial answer will be determined through experimental work. Indeed, the experimental maps will provide information about the control function used by nature to produce morphogenic events. On Figure 3 we represents a discretisation of a fractone map (obtained experimentally) with a prescribed precision (which is equivalent to choose the size of the units in our model). This discretised map will be used to extract information about the control function.

Restated in mathematical terms, we have:

> *Given $I_{t_0} \times J_{t_0}$ and $I_{t_f} \times J_{t_f}$, determine $X(t_0)$ and an admissible control $u(\cdot)$ such that $I_{t_0} \times J_{t_0}$ transforms into $I_{t_f} \times J_{t_f}$ under the evolution of system (4) and the rules for mitosis described in section 3.4.*

Due to the morphogenic nature of the system under study that implies a dynamic state space, this problem opens a completely new area in the field of control theory. New methods will have to be developed to answer such questions, and these type of problems are highly nontrivial. To understand the nature of the problem, we take a look at a simple case in Section 5.

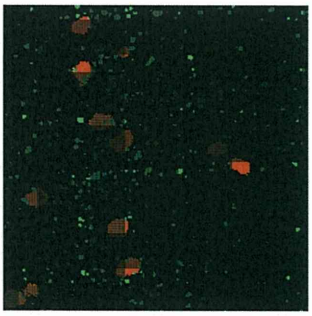

Figure 3: **Discretisation of a fractone map.**

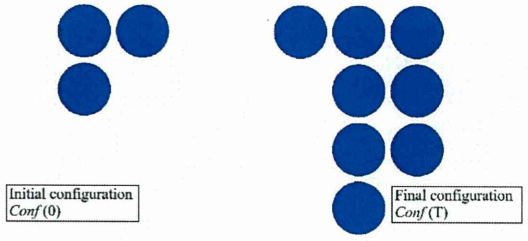

Figure 4: **Initial and final configuration of cells.** *For those configurations, there exist multiple sequences of morphogenic events to reach the desired configuration from the initial one.*

After stating the problem as above, we can go into more sophisticated versions. Indeed, as it can be seen in Section 5, there might not exist a solution to this problem for a given set of initial and final configurations. In this case, how do we modify the question? One solution is to introduce a notion of distance between configurations of cells and to ask how to reach a final configuration that is at the shortest distance from the desired one. There is also clearly the possibility that several controls lead to the same final configuration of cells. In that case, how do we select one? What is the criterion to be used to determine the most efficient control function? One strategy to be explored in a forthcoming work is based on the experimental observations collected in the lab through the fractone's maps. Based on those observations as well as assumptions such as minimizing the number of times mitosis can take place during the entire duration of the morphogenic event or minimizing the number of switching in the control function (which is equivalent to minimize the changes in the spatial distribution of the fractones), we can ascribe a cost function to be minimized. Our problem then becomes an optimal control problem. The bottom line is that, due to the complexity of the biological system that we study, there is an extremly large number of questions associated to this problem, and as said previously new methods need to be developed.

The current model is based on what we believe are the most critical features of our hypothesis. However, some of our assumptions are very restrictive and we also need to add some complexity to produce a more realistic model. For instance, to be added in the model in a forthcoming work is the following: first, we want to relax the assumption that the cells are horizontally and vertically aligned to allow broader configuration of cells; second, it is important to introduce a penality function for the diffusion of growth factors in the intracellular space found between the cells with respect to the diffusion in the free ambiant space; and third, we would like to add the possibility of having multiple growth factors diffusing in the ambiant space at different rates as well as having active fractones with varying sensitivities to each respective growth factor. However, despite the new features to be added, the statement of the problem will generally remain the same.

5. Example

On Fig. 4 we represent the desired initial and final configuration of cells, respectively $Conf(0)$ and $Conf(T)$. Let us at this stage not discuss the diffusion of growth factor but focus on the spatial distribution of fractones, i.e. on the control function that creates the morphogenic events to transform $Conf(0)$ into $Conf(T)$. Also, to limit complexity, we assume that there is only one fractone active at a time. We have that:
$I_0 \times J_0 = \{-20, \cdots, 22\} \times \{-30, \cdots, 12\} \backslash (A \cup B)$ where $A = \{-9, \cdots, 1\} \times (\{-9, \cdots, 1\} \cup \{1, \cdots, 9\})$ and $B = \{1, \cdots, 9\} \times \{1, \cdots, 9\}$ and $I_T \times J_T = I_0 \times J_0 \backslash (C \cup D \cup E)$ where we have $C = \{-19, \cdots, -11\} \times \{1, \cdots, 9\}$, $D = \{-9, \cdots, -1\} \times (\{-29, \cdots, -21\} \cup \{-19, \cdots, 11\})$ and $E = \{1, \cdots, 9\} \times (\{-19, \cdots, -11\} \cup \{-9, \cdots, -1\})$.
Notice that we arbitrarily choose the origin of our discretisation as the unit between the three initial cells and that the ambiant space is assumed to be a square, each side being composed of 42 units. Assume, for instance, that an active fractone is located in unit $(-10, -10)$ and that it reaches the threshold value for duplication, then the mass of cells transforms into four cells in a square configuration. In other words, we have $I_{t_1} \times J_{t_1} =$ where t_1 is the time needed for the stored concentration of growth factor in the unit associated to the active fractone to reach the threshold. The following control function $u(\cdot)$, where the time duration for each piecewise constant component depends on the diffusion process of the growth factor, generates morphogenic events starting with the prescribed configuration and reaching the desired one:
(8)

$$u(t) = \begin{cases} u_{(-10,-10)}(t) = 1, \text{ and 0 otherwise for } 0 \leq t < t_1 \\ u_{(-10,0)}(t) = 1, \text{ and 0 otherwise for } t_1 \leq t < t_2 \\ u_{(-10,-20)}(t) = 1, \text{ and 0 otherwise for } t_2 \leq t < t_3 \\ u_{(-10,-20)}(t) = 1, \text{ and 0 otherwise for } t_3 \leq t \leq T \end{cases}$$

A graphic representation can be seen on Fig. 5. It is easy to see that the control is not unique, i.e. there is another sequence of morphogenic events leading to the same desired cell configuration.

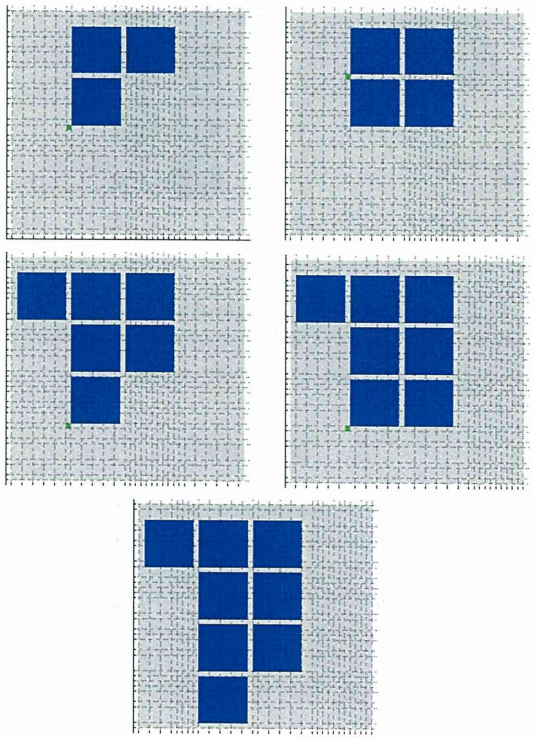

Figure 5: **Morphogenic Events Starting as** $Conf(0)$ **and reaching** $Conf(T)$. *Notice that each step between pictures incorporates duplication of cells as well as a possible change in the distribution of the active fractone.*

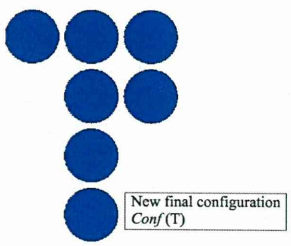

Figure 6: **Representation of the perturbed final configuration.** *Notice that it differs only by one cell from the previous one. In this case, there exists no morphogenic event based on our assumptions for mitosis that can lead exactly to this configuration.*

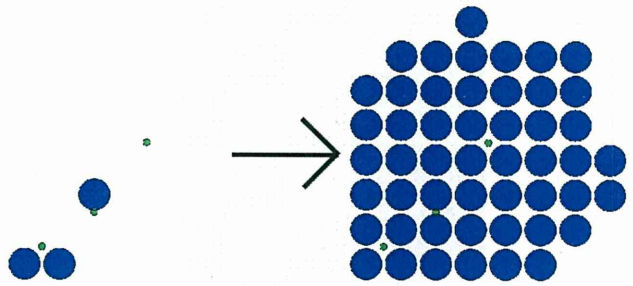

Figure 7: **Initial and Final Configurations for a series of Morphogenic Events.**

Let us now perturbe very slightly the desired configuration of cells, see Fig 6, i.e. we take $\tilde{I}_T \times \tilde{J}_T = I_T \times J_T \cup \{1, \cdots, 9\} \times \{-19, \cdots, -11\}$. In that case, given the rules for mitosis from section 3.4, it can be shown that there is no spatial distribution of fractones to solve the problem (in other words there is no admissible control function $u(.)$). However, as seen previously, there is an admissible control to reach the final configuration displayed in Fig. 4. This configuration differs from the desired one by only one cell. As suggested above, it will therefore makes sense to introduce in the future a notion of distance between configurations of cells and to ask how to reach a final configuration that is at the shortest distance from the desired one.

On Figure 7, we represent an initial configuration with 3 cells and 3 fractones and its final configuration after a series of morphogenic events. Notice that the square shape of the final mass of cells on thebottom left is due to the fact that the boundary of the ambiant space is fixed. This can easily be relaxed if necessary.

6. Future Work

There are mainly two directions of work that we are planning to undertake at this stage. First, from a purely mathematical perspective an open question is the development of new techniques to answer controllability and optimality questions for control systems such as the one introduced in this paper. Second, the interplay between the biological motivation and the mathematics must be refined to predict neurulation and post-neurulation growth by the mathematical model using fractone maps. More precisely, we need to first incorporate into the model important features that have not yet been taken into account. During the same time, we will use dual and triple immunocytochemistry for laminin (fractone marker) and for phosphorylated histone-3/bromodeoxyuridine (both markers of proliferating cells) and epifluorescence microscopy recording to map fractones and cell proliferation throughout the developing brain from embryonic stage E7.5 to E14.5. Then, after discretizing the fractone maps, we will determine whether the prediction of the mathematical model reflects the growth of the neural tissue observed in the maps. The observation of spatial dis-

tribution of fractones provided by the maps will determine the control function to be used in the mathematical model to produce our simulations.

Acknowledgments

This work was supported by the National Science Foundation, award DUE-0634624, "UBM-Institutional: Research Experiences in Mathematical Biology", and by NIH grant R21 NS057675 and NIH/NCRR 5 G12 RR/AI03061.

References

[1] Aviezer, D., Hecht, D., Safran, M., Elsinger, M., David, G., and Yayon, A. Perlecan, basal lamina proteoglycan, promotes basic fibroblast growth factor-receptor binding, mitogenesis and angiogenesis. *Cell.* **79**:1005-1013, 1994.

[2] Brickman, Y.G., Ford M.D., Small D.H., Bartlett P.F., and Nurcombe, V. Heparan sulfates mediate the binding of basic fibroblast growth factor to a specific receptor on neural precursor cells. *J. Biol. Chem.* **270**, 24941-24948, 1995.

[3] Cannon W.B. *The wisdom of the body.* New York: Norton, 1932.

[4] *Autonomous Underwater vehicles Ocean Engineering*, Special Issue on Autonomous Underwater Vehicles, Chyba, M.: Guest Editor, Vol 36/1, pp. 1-132, 2009.

[5] Chyba, M., Haberkorn, T., Smith, R.N., and Choi S.K. Autonomous Underwater Vehicles: Development and Implementation of time and Energy Efficient Trajectories. *Ship Technology Research*, **55/2**, pp.36-48, 2008.

[6] Douet, V. and Mercier, F. *Investigating the role of the extracellular matrix structures fractones as captors and modulators of growth factor activity in the adult neurogenic zone.* Submitted to Integrative Biology.

[7] Gordon, M.Y., Riley, G.P., Watt, S.M., and Greaves, M.S. Compartmentalization of a hematopoeitic growth factor (GM-CSF) by glycosamino glycans in the bone marrow microenvironment. *Nature.* **326**:403-405, 1987.

[8] Hannon, B. and Ruth M. *Modeling Dynamic Biological Systems.* Springer-Verlag, Series : Modeling Dynamic Systems, New York, 1997

[9] Kalman, R.E. *On the General Theory of Control Systems.* Proceedings First International Conference on Automatic Control, Moscow, USSR, 1960.

[10] Kerever, A., Schnack, J., Vellinga, D., Ichikawa, N., Moon, C., Arikawa-Hirasawa, E., Efird, J.T., and Mercier, F. *Novel extracellular matrix structures in the neural stem cell niche capture the neurogenic factor fibroblast growth factor 2 from the extracellular milieu.* Stem Cells **25**:2146-2157, 2007.

[11] Leivo, I., Vaheri, A., Timpl, R., and Wartiovaara, J. *Appearance and distribution of collagens and laminin in the early mouse embryo.* Dev Biol **76**:100-114, 1980.

[12] Leivo, I. and Wartiovaara, J. Basement membrane matrices in mouse embryogenesis, teratocarcinoma differentiation and in neuromuscular maturation. *Int J Dev Biol* **33**:81-89, 1989.

[13] Mercier, F., Kitasako, J.T., and Hatton, G.I.. Anatomy of the brain neurogenic zones revisited: fractones and the fibroblast/macrophage network. *J Comp Neurol* **451**:170-188, 2002.

[14] Mercier, F., Kitasako, J.T., and Hatton, G.I. Fractones and other basal laminae in the hypothalamus. *J Comp Neurol* **455**:324-340, 2003.

[15] Nurcombe V, Fond MD, Wildschut J, Bartlett PF. *Developmental regulation of neural response to FGF-1 and FGF-2 by heparan sulfate proteoglycan.* Science **260**, 103-106, 1993.

[16] B. Piccoli and M. Garavello *Traffic Flow on Network*, AMS book series, Applied Math Series n. 1, American Institute of Mathematical Sciences, 2006.

[17] Roberts, R., Ghallager, J., Spooncer, E., Allen, T.D., Bloomfield, F., Dexter, T.M. *Heparan sulfate-bound growth factor: a mechanism for stromal cell mediated hematopoiesis.* Nature. **332**:376-378, 1988.

[18] Sontag E.D.. *Some new directions in control theory inspired by systems biology.* IET Systems Biology, **1**:9-18, 2004.

[19] Sontag, E.D. Molecular systems biology and control. *Eur. J. Control*, **11(4-5)**:396-435, 2005.

[20] Stewart G.R., Pearlman A.L. Fibronectin-like immunoreactivity in the developing cerebral cortex. *J Neurosci* **7**:3325-3333, 1987.

[21] Turing AM. *The chemical basis of morphogenesis.* Phil Trans R Soc Lond B Biol Sci **237**: 37-72, 1952.

[22] Von Bertalanffy, L. *General System theory: Foundations, Development, Applications.* George Braziller. 1968.

[23] Wartiovaara J., Leivo I., Virtanen I., Vaheri A., Graham C.F. *Appearance of fibronectin during differentiation of mouse teratocarcinoma in vitro.* Nature **272**: 355-356, 1978.

[24] Wartiovaara J., Leiva I., Vaheri A. *Expression of the cell surface-associated glycoprotein, fibronectin, in the early mouse embryo.* Dev. Biol. **69**: 247-257, 1979.

[25] Wiener N. *The Extrapolation, Interpolation and Smoothing of Stationary Time Series.* John Wiley and Sons, Inc., New York, N.Y., 1949.

[26] Yayon, A., Klagsbrun, M., Esko, J.D. Leder, P., Ornitz, D.P. Cell surface, heparin-like molecules are required for binding of basic fibroblast growth factor to its high affinity receptor. *Cell.* **64**:841-848, 1991.

Monique Chyba, John Rader, Youngsu Chow Kwon and Rich Kodama
Department of Mathematics, 2565 Mc Carthy Mall, University of Hawaii, Honolulu, HI 96822, USA
E-mail: chyba(at)math.hawaii.edu
jrader(at)hawaii.edu
youngsu(at)hawaii.edu
rtkodama(at)hawaii.edu

Frederic Mercier
Pacific Biosciences Research Center, University of Hawaii, Biomed T401, 1960 East-West rd, Honolulu, HI 96822, USA
E-mail: fmercier(at)pbrc.hawaii.edu

Vanessa Douet
Department of Neurology, Jutendo School of Medicine, Tokyo, Japan; and Pacific Biosciences Research Center, University of Hawaii, Honolulu, USA
E-mail: vanessa(at)juntendo.ac.jp

Eri Arikawa-Hirasawa
Department of Neurology, Juntendo School of Medicine, Tokyo, Japan
E-mail: ehirasaw(at)juntendo.ac.jp

Matrix Biology 31 (2012) 17–28

Contents lists available at SciVerse ScienceDirect

Matrix Biology

journal homepage: www.elsevier.com/locate/matbio

Laminin α1 is essential for mouse cerebellar development

Naoki Ichikawa-Tomikawa [a,e], Junko Ogawa [a,d], Vanessa Douet [a], Zhuo Xu [a], Yuji Kamikubo [b], Takashi Sakurai [b], Shinichi Kohsaka [d], Hideki Chiba [e], Nobutaka Hattori [c], Yoshihiko Yamada [f], Eri Arikawa-Hirasawa [a,c,*]

[a] Research Institute for Diseases of Old Age, Juntendo University Graduate School of Medicine, Tokyo, Japan
[b] Department of Pharmacology, Juntendo University Graduate School of Medicine, Tokyo, Japan
[c] Department of Neurology, Juntendo University Graduate School of Medicine, Tokyo, Japan
[d] National Institute of Neuroscience, National Center of Neurology and Psychiatry, Tokyo, Japan
[e] Department of Basic Pathology, Fukushima Medical University School of Medicine, Fukushima, Japan
[f] National Institute of Dental and Craniofacial Research, NIH, Bethesda, MD, USA

ARTICLE INFO

Article history:
Received 19 June 2011
Received in revised form 13 September 2011
Accepted 16 September 2011

Keywords:
Laminin α1 chain
Meninges
Cerebellum

ABSTRACT

Laminin α1 (Lama1), which is a subunit of laminin-1 (laminin-111), a heterotrimeric ECM protein, is essential for embryonic development and promotes neurite outgrowth in culture. Because the deletion of Lama1 causes lethality at early embryonic stages in mice, the in vivo role of Lama1 in neural development and functions has not yet been possible to determine. In this study, we generated conditional *Lama1* knockout (*Lama1*^{CKO}) mice in the epiblast lineage using *Sox2-Cre* mice. These *Lama1*^{CKO} mice survived, but displayed behavioral disorders and impaired formation of the cerebellum. Deficiency of Lama1 in the pial basement membrane of the meninges resulted in defects in the conformation of the meninges. During cerebellar development, Lama1 deficiency also caused a decrease in the proliferation and migration of granule cell precursors, disorganization of Bergmann glial fibers and endfeet, and a transient reduction in the activity of Akt. A marked reduction in numbers of dendritic processes in Purkinje cells was observed in *Lama1*^{CKO} mice. Together, these results indicate that Lama1 is required for cerebellar development and functions.

1. Introduction

Two principal neuronal cell types, Purkinje and granule cells, are essential for the normal development and functioning of the cerebellum. Purkinje cells, which develop first, migrate along the radial glial system from the germinative zone. In contrast, granule neurons migrate from the proliferative zone in the external granule layer (EGL) to the internal granule layer (IGL), guided by Bergmann glial processes (Rakic and Sidman, 1973; Herrup and Kuemerle, 1997; Hatten, 1999).

Extracellular matrix (ECM) proteins and their receptors closely participate in cerebellar development. For example, vitronectin, is expressed in differentiated granule neurons and acts to decrease sonic hedgehog-induced proliferation of granule cell precursors (GCPs) and to promote neural differentiation (Pons et al., 2001). In mice, CNS-specific knockout of integrin β1, one of the major receptors of ECM proteins, and of its downstream molecules, integrin-linked kinase (ILK) and focal adhesion kinase (FAK), causes defects in the formation of folia by decreasing the proliferation of GCPs and causes abnormalities in the formation of Bergmann glia and Purkinje cells (Graus-Porta et al., 2001; Blaess et al., 2004; Mills et al., 2006; Watanabe et al., 2008). Other ECM protein receptors, α- and β-dystroglycan, regulate the migration of cerebellar granule neurons (Qu and Smith, 2004; Satz et al., 2010).

Laminins comprise a family of heteromeric ECM proteins consisting of α, β, and γ chains (Miner and Yurchenco, 2004; Aumailley et al., 2005). Laminins are required for basement membrane assembly (Li et al., 2003; Li et al., 2005), and they regulate cellular behavior through interactions with cell surface receptors, including integrins, syndecans, and α-dystroglycan (Gullberg and Ekblom, 1995; Miner and Yurchenco, 2004). Laminin α1 (Lama1) is the first laminin to be expressed during mouse embryogenesis (Smyth et al., 1999; Miner et al., 2004) and in vitro studies have demonstrated it to have a number of biological activities, including promotion of cell adhesion, migration, neurite outgrowth, angiogenesis, and tumor metastasis (Kleinman et al., 1990; Ekblom et al., 2003; Ichikawa et al., 2009). Mouse embryos that are deficient in Lama1 lack Reichert's membrane and die by embryonic day 7 (E7) (Miner et al., 2004; Alpy et al., 2005). Mutant mice expressing a truncated Lama1 lack the C-terminal LG4 and LG5 subdomains and die before E6.5, despite the presence of both the embryonic basement membrane and Reichert's membrane

Abbreviations: CKO, conditional *Lama1* knockout; CNS, central nervous system; Cont, control; ECM, extracellular matrix; EGL, external granule layer; GCPs, distorted the layer granule cell precursors; IGL, internal granule layer.

* Corresponding author at: Juntendo University Graduate School of Medicine, Research Institute for Diseases of Old Age, Building 10, Room 606, 2-1-1 Hongo, Bunkyo-ku, Tokyo 113-8421, Japan. Tel./fax: +81 3 3814 3016.
E-mail address: ehirasaw@juntendo.ac.jp (E. Arikawa-Hirasawa).

0945-053X/$ – see front matter © 2011 Elsevier B.V. All rights reserved.
doi:10.1016/j.matbio.2011.09.002

(Scheele et al., 2005). A missense mutation and conditional knockout of the *Lama1* gene in mice disrupt retinal vascular development and inner limiting membrane formation (Edwards et al., 2010).

Although Lama1 is present in the meninges and in larger vessels in the late developmental stages of the CNS (Andrae et al., 2004), the in vivo role of Lama1 in the CNS is unknown. In this report, we created conditional null mice using epiblast-specific Sox2-Cre and found that Lama1 was essential for the proliferation and migration of GCPs in the cerebellum. Lama1 was also required for formation of Bergmann glial processes and for the localization and dendritic formation of Purkinje cells.

2. Results

2.1. Generation of conventional and conditional Lama1-knockout mice

To generate conventional ($Lama1^{KO}$) and conditional ($Lama1^{CKO}$) *Lama1 null* mice, two ES clones were isolated by transfecting the targeting vector, which contained the PGK-neo^r-PGK-tk cassette flanked by two loxP sequences in intron 15 and a third loxP sequence in intron 17 of the *Lama1* allele (Supplementary material Fig. S1A). These cells were transiently transfected with a CMV-Cre expression plasmid, and ES clones containing either the *Lama1*-deleted allele or floxed allele were obtained. The ES clones from each were injected into blastocysts to generate either $Lama1^{KO}$ or floxed-*Lama1* mice. Homozygous $Lama1^{KO}$ ($Lama1^{del/del}$) mice died by embryonic day 7 (E7) because of the absence of Reichert's membrane (data not shown), similar to *Lama1* null mice described in a previous report (Miner et al., 2004; Alpy et al., 2005). *Lama1* mRNA and protein were absent in homozygous $Lama1^{KO}$ mice (data not shown). Southern blotting and genomic PCR confirmed the genotype of $Lama1^{KO}$ mice (Supplementary material Fig. S1B). The floxed-*Lama1* ($Lama1^{flox/flox}$) mice were fertile and phenotypically normal. To identify the role of Lama1 in tissue development and functions at later stages, we created $Lama1^{CKO}$ ($Lama1^{flox/del}$; $Sox2^{cre/+}$) mice by crossing floxed-*Lama1* mice with *Sox2-Cre* transgenic mice. The Sox2 gene is expressed in the inner cell mass, epiblast, and extraembryonic ectoderm prior to gastrulation, and in the prospective neural plate and chorion at the onset of gastrulation. All epiblast cells appear to have undergone a recombination event of *Sox2-Cre* by E6.5 (Hayashi et al., 2002). $Lama1^{CKO}$ mice underwent complete gestation and survived postnatally. Both genders of $Lama1^{CKO}$ mice showed normal sexual development and fertility. A genomic PCR analysis demonstrated that the floxed segment of the floxed-*Lama1* allele was almost completely deleted in the tail of $Lama1^{CKO}$ mice (Supplementary material Fig. S1C), and that this deleted allele was detected in almost all adult tissues (Supplementary material Fig. S1D). Subsequent RT-PCR analysis revealed the absence of *Lama1* mRNA in the cerebellum of $Lama1^{CKO}$ mice (Supplementary material Fig. S1E).

2.2. $Lama1^{CKO}$ mice display abnormal behaviors

Three behavioral tests were conducted to determine whether $Lama1^{CKO}$ mice have abnormalities in behavior: the tail suspension test, the rotarod test, and footprint analysis. In the tail suspension test, $Lama1^{CKO}$ mice showed hugging behavior whereas control $Lama1^{flox/del}$ mice showed normal escape-oriented movements: running forward and backwards, body torsions with attempts to catch the suspended body (Fig. 1A). In the rotarod test, the movement time of $Lama1^{CKO}$ mice was shorter than that of control mice, indicating that $Lama1^{CKO}$ mice have motor deficits (Fig. 1B). In the footprint test, $Lama1^{CKO}$ mice showed a significant reduction in stride length and an increase in interlimb coordination when compared with control mice, indicating the occurrence of locomotion disorder in $Lama1^{CKO}$ mice (Fig. 1C). These behavioral abnormalities suggest the occurrence of defects in neuronal functions, which result in the disequilibrium and lack of coordination seen in $Lama1^{CKO}$ mice.

2.3. Reduced size and structural defects in the cerebellum of $Lama1^{CKO}$ mice

For further investigation of the neurological dysfunction, we analyzed histological sections of the brains of adult $Lama1^{CKO}$ mice. The cerebellum was reduced in size and the superior colliculus was appreciably exposed to the surface of the brain compared to the situation in control $Lama1^{flox/del}$ mice (Supplementary material Fig. S2). To analyze the morphological changes in the cerebellum in more detail, we examined sagittal sections stained with Luxol Fast Blue (Fig. 2A and B). In the cerebellum of $Lama1^{CKO}$ mice, the depth of folia decreased and aggregation of granule cells appeared at the cerebellum surface, along the line of fusion of adjacent cerebellar folia under the meninges (arrows in Fig. 2Ba and b). The meninges, which form the fissures of folia, were not in the correct location in $Lama1^{CKO}$ mice (asterisk in Fig. 2Bc). These results suggest that the behavioral dysfunctions seen in $Lama1^{CKO}$ mice are due at least in part to cerebellar defects.

2.4. Defects in the arrangement and dendritic processes in Purkinje cells

Purkinje cells, which are the main neuronal cells in the cerebellum, originate in the ventricular zone and migrate to the cortex along the radial glial fiber. After this migration, Purkinje cells form a cell layer and extend axons and dendrites (Goldowitz and Hamre, 1998). During postnatal development, Purkinje cell dendrites form synaptic contacts with parallel and climbing fibers in the molecular cell layer (Sotelo, 2004). Because of the remarkable abnormality in the cerebellar formation observed in $Lama1^{CKO}$ mice, we examined the layer formation and neurite extension of Purkinje cells by staining 50 μm thick sections of the cerebellum with an antibody to calbindin, a marker of Purkinje cells (Fig. 3). In $Lama1^{CKO}$ mice at P0, P10, and adult stages, the layer of Purkinje cells was distorted, and the localization of some Purkinje cells was away from the cell layer (Fig. 3A, asterisks). The formation of the dendritic tree of Purkinje cells in the folia of $Lama1^{CKO}$ mice at P5, P10, and adult stages was reduced compared to that of control Purkinje cell dendrites (Fig. 3B, asterisks).

2.5. The expression of Lama1 and other ECM molecules in the meningeal basement membrane

Lama1 is expressed in the meningeal basement membrane at the surface of the brain, from the late embryonic stage to adulthood (Supplementary material Fig. S3). Previous reports also indicated that other laminin α chains, including α2 (Lama2), α4 (Lama4), and α5 (Lama5), are expressed in the meningeal basement membrane (Andrae et al., 2004; Blaess et al., 2004). Because other ECM molecules may compensate for the deletion of Lama1 in $Lama1^{CKO}$ mice, we examined the expression and localization of several ECM molecules in normal looking cerebellar areas of P5 $Lama1^{CKO}$ mice by immunostaining. In $Lama1^{CKO}$ mice, no expression of Lama1 was detected, consistent with the RT-PCR and immunostaining results (Supplementary material Fig. S1E and Fig. 4A), but Lama2 and Lama5 were present in the meningeal basement membrane of $Lama1^{CKO}$ mice (Supplementary material Fig. S4A and C). The expression level of Lama2 was slightly increased, whereas that of Lama5 was decreased in the mutant mice. Lama4 was present in the blood vessel basement membrane and its expression level did not change between $Lama1^{CKO}$ and control $Lama1^{flox/del}$ mice (Supplementary material Fig. S4B). Nidogen-1, another ECM molecule, was expressed in both the meningeal and blood vessel basement membrane of $Lama1^{CKO}$ mice, and its expression level was the same as that in control mice (Supplementary material Fig. S4B). Integrin β1, a main receptor of laminin α chains, was present in the endothelial cells of $Lama1^{CKO}$ mice, and no significant differences were noted between mutant and control mice (Supplementary material Fig. S4C). These results indicate

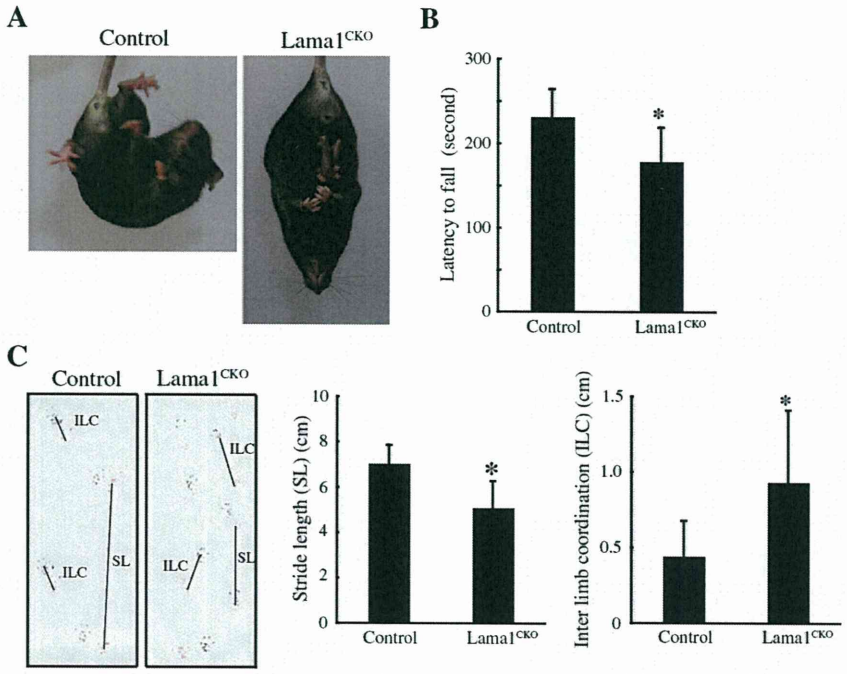

Fig. 1. Impaired behavior of Lama1^{CKO} mice. (A) Tail suspension test of adult mice. *Lama1*^{CKO} mice exhibit hugging behavior. (B) RotaRod performance at 8–15 weeks of age. *Lama1*^{CKO} mice show a marked decrease in latency to fall as compared with control *Lama1*$^{flox/del}$ mice. The bar graph shows the mean and SD of time to fall (n = 10) (*, $P<0.001$; two-sided *t*-test) (C) Representative footprints of control and *Lama1*^{CKO} mice. *Lama1*^{CKO} mice showed a significant reduction in stride length (SL) and increase in interlimb coordination (ILC) compared with control *Lama1*$^{flox/del}$ mice. The graphs show the mean and SD of length. (n = 5) (*, $P<0.001$; two-sided *t*-test).

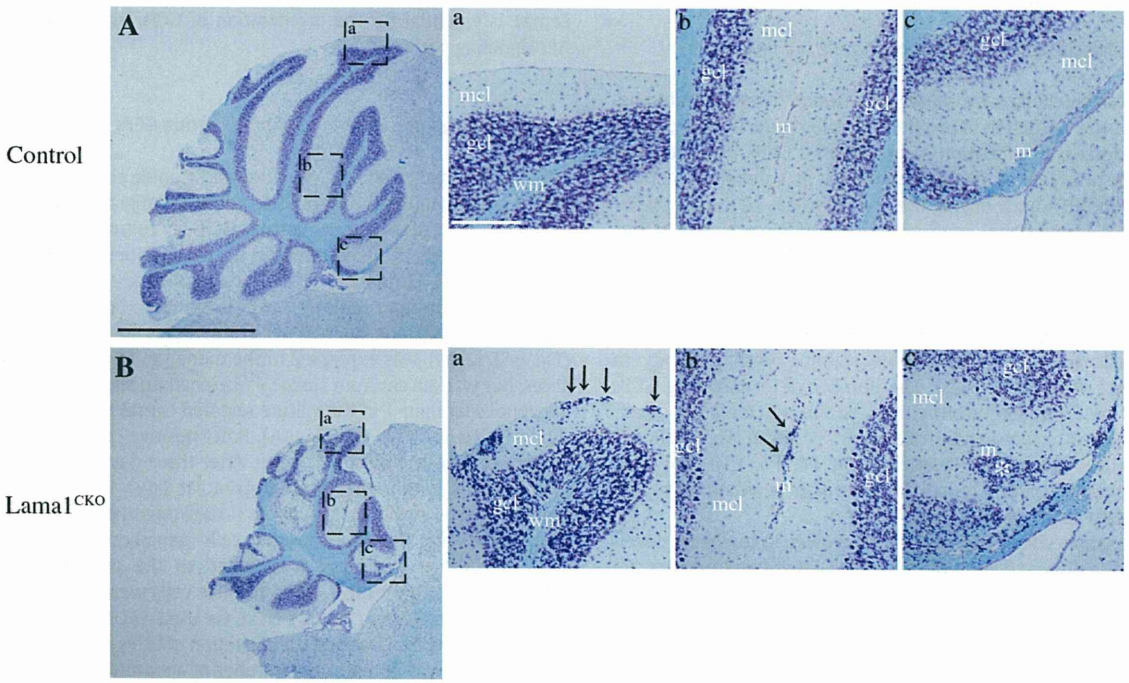

Fig. 2. Cerebellar defects in Lama1^{CKO} mice. Sagittal sections of adult control (A) and *Lama1*^{CKO} mice at 8 weeks age (B) were stained with Luxol Fast Blue. The cerebellum of *Lama1*^{CKO} mice is smaller than that of control mice, and the formation of some folia is disrupted. (a–c) High magnification view of areas indicated. In *Lama1*^{CKO} mice, the aggregation of granule cells in the molecular layer was observed under meninges of the cerebellar surface and fusion lines of folia (arrows). The meninges, which form the fissure of the folia, were completely lacking (asterisk). mcl, molecular cell layer; gcl, granule cell layer; wm, white matter; m, meninges. Black scale bars: 1.0 mm, White scale bars: 100 μm.